

JETS AND WIDE ANGLE OUTFLOWS IN CEPHEUS E: NEW EVIDENCE FROM *SPITZER*

T. VELUSAMY¹, W. D. LANGER¹, M. S. N. KUMAR², J. M. C. GRAVE²

Draft version August 19, 2011

ABSTRACT

Outflows and jets are believed to play a crucial role in determining the mass of the central protostar and its planet forming disk by virtue of their ability to transport energy, mass, and momentum of the surrounding material, and thus terminate the infall stage in star and disk formation. In some protostellar objects both wide angle outflows and collimated jets are seen, while in others only one is observed. *Spitzer* provides unprecedented sensitivity in the infrared to study both the jet and outflow features. Here, we use HiRes deconvolution to improve the visualization of spatial morphology by enhancing resolution (to sub-arcsecond levels in the IRAC bands) and removing the contaminating sidelobes from bright sources. We apply this approach to study the jet and outflow features in Cep E a young, energetic Class 0 protostar. In the reprocessed images we detect: (i) wide angle outflow seen in scattered light; (ii) morphological details on at least 29 jet driven bow shocks and jet heads or knots; (iii) three compact features in 24 μm continuum image as atomic/ionic line emission coincident with the jet heads; and, (iv) a flattened $\sim 35''$ size protostellar envelope seen against the interstellar background PAH emission as an absorption band across the protostar at 8 μm . By separating the protostellar photospheric scattered emission in the wide angle cavity from the jet emission we show that we can study directly the scattered light spectrum. We present the H₂ emission line spectra, as observed in all IRAC bands, for 29 knots in the jets and bowshocks and use them in the IRAC color – color space as a diagnostic of the thermal gas in the shocks driven by the jets. The data presented here will enable detailed modeling of the individual shocks retracing the history of the episodic jet activity and the associated accretion on to the protostar. The *Spitzer* data analysis presented here shows the richness of its archive as a resource to study the jet/outflow features in H₂ and scattered light in a large homogeneous sample.

Subject headings: infrared: general — star formation: protostar — ISM: jets and outflows

1. INTRODUCTION

Star formation begins with the collapse of a dense interstellar cloud core to a protostar surrounded by a disk of gas and dust. The envelope of the cloud core falls inwards to feed further growth of the protostar and its accreting disk. At some point during the accretion phase, protostellar jets and winds originate close to the surface of the forming star and interact with the dense envelope surrounding the protostar-disk system (e.g. Königl & Pudritz 2000; Shu et al. 2000). These outflows and jets are believed to play a crucial role in determining the mass of the central protostar and its planet forming disk by virtue of their ability to transport energy, mass, and momentum of the surrounding material, and thus terminate the infall stage in star and disk formation. It is now well recognized that jets and outflows are essential and inherent to the star formation process. These flows are broadly classified into two types: molecular outflows traced mainly with CO emission, and jets observed by optical emission (cf. recent reviews by Arce et al. 2007, Pudritz et al. 2007; Bally 2007). Observations indicate that around some protostars, high-velocity jets with a narrow opening angle are enclosed by a low-velocity outflow with a wide opening angle (e.g. Mundt & Fried 1983;

Velusamy et al. 2007) however, in others only one component is observed. Poorly collimated flows can be due to extreme precession of the jet (Shepherd et al. 2000) and indistinguishable from wide angle outflows. The wide angle outflows, which are also observed in the scattered light, are often missed in the optical or near-IR due to instrument insensitivity to faint emission and confusion from the bright protostellar emissions. *Spitzer* provides unprecedented sensitivity in the infrared to detect the jet/outflow features. The IRAC, IRS, and MIPS observations can provide new insight into the structure, morphology, and physical and chemical characteristics of the outflow sources as demonstrated in the observations of HH46/47 by Noriega-Crespo et al. (2004a) & Velusamy et al. (2007), Cep E by Noriega-Crespo et al. (2004b), L1512F by Bourke et al. (2006), L1448 by Tobin et al. (2007) & Dionatos et al. (2009), L1251 by Lee et al. (2010), and HH211 by Dionatos et al. (2010). Using the IRAC colors alone, Ybarra & Lada (2009) demonstrated the feasibility to study the pure rotational H₂ line emissions in the shocks without the need for spectroscopic data. Velusamy et al. (2007) demonstrated that resolution enhanced re-processing of *Spitzer* images in the case of HH46/47 brought out more clearly the morphologies of: (a) wide-angle outflow cavities in the IRAC 3.6 & 4.5 μm images by scattered starlight, (b) jets and bow shocks in H₂ molecular emission within the IRAC bands, and (c) the hottest atomic/ionic gas in the jet head characterized by [Fe II] and [S I] line emissions within the MIPS 24 μm band.

¹ Jet Propulsion Laboratory, California Institute of Technology, 4800 Oak Grove Drive, Pasadena, CA 91109; velusamy@jpl.nasa.gov, William.D.Langer@jpl.nasa.gov

² Centro de Astrofísica da Universidade do Porto, Rua das Estrelas, 4150-762 Porto, Portugal; nanda@astro.up.pt, jgrave@astro.up.pt

In this paper we present new results on Cep E obtained by reprocessing the *Spitzer* IRAC and MIPS images with the HiRes deconvolution (Backus et al. 2005). Cep E is a remarkably bright outflow object, at a distance of 730 pc, with strong radiative power ($\sim 80 L_{\odot}$), and appears to be an intermediate mass object which is expected to reach a final stellar mass of $3M_{\odot}$ (Froebrich et al. 2003). Cep E has been recently classified as a Class 0 protostar by Noriega-Crespo et al. (2004b) based on the *Spitzer* Early Release Observations. It is among the youngest protostars with an age in the range of 20 – 400 thousand years, estimated for different evolutionary models (Froebrich, 2005; and the references therein). In the near- and mid-IR its morphology is similar to that expected for a jet driven outflow, where the leading bow shocks entrain and accelerate the surrounding molecular gas. The properties of this outflow have been well studied by Moro-Martín et al. (2001) and Smith et al. (2003). The southern bright bowshock, identified as HH 377 (Devine, Reiputh & Bally 1997), is well studied in the optical wavelengths using the [O I] λ 6300, [N I] λ 5200 and [S II] $\lambda\lambda$ 6717,6731 lines tracing the dissociative shocks characteristics of HH flows (e.g. Ayala et al. 2000) and later in the near-IR in the [Fe II] 1.26 and 1.64 μ m emission lines, utilizing the fact that [S II] and [Fe II] have very similar excitation energies (Nisini et al. 2002). Furthermore, Hartigan, Raymond & Hartmann 1987) interpreted the relative strength of [O I] and [N I] with respect to H_{α} and the lack of [O II] and [O III] in terms of relatively low velocity (20-25 km s $^{-1}$) dissociative shocks and concluded that the south bowshock of Cep E is a low excitation HH object. In addition to dissociative shocks, the HH outflows are known to have also magnetic precursors (C-shocks) needed to explain excitation of the molecular H_2 emission. Cep E lobes have been well imaged in H_2 emission in IR: in $v=1-0$ S(1) 2.122 μ m; $v=2-1$ S(1) 2.248 μ m; $v=3-2$ S(3) 2.202 μ m (Eisloffel et al. 1996; Ladd & Hodapp, 1997); $v=0-0$ S(5) 6.91 μ m and S(3) 9.66 μ m (Noriega-Crespo 1998); $v=1-0$ S(1) 1.21 μ m. In the mid-IR a series of 6 pure rotational emission lines H_2 0-0 S(2) to S(7) in the wavelength range of 12.28 μ m to 5.51 μ m in the Cep E lobes were first imaged by ISOCAM CVF (Moro-Martín et al. 2001) and their excitation diagrams led to the use of H_2 line ratios as C-shock diagnostics. The emissions in the *Spitzer* images in all the IRAC bands are dominated by a wide range of H_2 rotational transitions from 0-0 S(4) to 0-0 S(13) and a few vibrational 1-0 transitions in the 3.6 μ m band. Thus *Spitzer* observations of Cep E enhance the rich data set already available in optical, near-IR and mm wavelengths. Furthermore, all the interpretations so far have focused on treating this object as having jets and bow shocks, but no wide angle outflow. Because of the limited spatial resolution even the CO outflow morphology has been interpreted as entrained low velocity molecular gas associated with the bow shock driven by the jets (Moro-Martín et al. 2001). Our enhanced image analysis show the simultaneous presence of wide angle outflow along with the bow shocks powered by the jets. In this paper we highlight the morphological features in the low velocity wide angle outflow and the high velocity jets and discuss a wide range of structures from compact knots to extended envelopes as seen in the reprocessed *Spitzer* IRAC and MIPS images.

2. ANALYSIS

Noriega-Crespo et al. (2004b) presented the mosaic images of Cep E in the *Spitzer* IRAC bands at 3.5 μ m, 4.5 μ m and 8 μ m in a three color representation and the mosaic image of MIPS band at 24 μ m. However, some of the structures were missed in these mosaic maps due to either lower spatial resolution or diffraction lobes. *Spitzer* provides unprecedented sensitivity in the infrared, but the spatial resolution is limited by the relatively small aperture (0.85 m) of the primary mirror. To maximize the scientific return of *Spitzer* images we use the HiRes deconvolution processing technique that makes the optimal use of the spatial information in the observations. The algorithm, “HiRes” and its implementation has been discussed by Backus et al. (2005) and its performance on a variety of astrophysical sources observed by *Spitzer* is presented by Velusamy et al. (2008). The HiRes deconvolution algorithm is based on the Richardson-Lucy algorithm (Richardson 1972; Lucy 1974), and the Maximum Correlation Method employed by Aumann et al. (1990) for IRAS data. As demonstrated by Velusamy et al. (2007; 2008) the HiRes deconvolution on *Spitzer* images retains a high fidelity preserving all the main features. HiRes deconvolution improves the visualization of spatial morphology by enhancing resolution and removing the contaminating sidelobes from bright sources. The benefits of HiRes include: (a) enhanced resolution $\sim 0.6'' - 0.8''$ for IRAC bands; $\sim 1.8''$ and $\sim 7''$ for MIPS 24 μ m and 70 μ m, respectively; (b) the ability to detect sources below the diffraction-limited confusion level; (c) the ability to separate blended sources, and thereby provide guidance to point-source extraction procedures; (d) an improved ability to show the spatial morphology of resolved sources. We reprocessed the images at all the IRAC bands and the MIPS 24 and 70 μ m bands using all available map data in these bands in the *Spitzer* archives containing the protellar object Cep E centered at ($\alpha = 23^h03^m12.5^s$, $\delta = +61^{\circ}42'30''$ [J2000]). We used the pipeline processed basic calibrated data (BCD) downloaded from the *Spitzer* Science Center (SSC) archives. We constructed mosaic images at each band using the MOPEX software (provided by SSC). In addition, we also produced reprocessed images at each band by applying the HiRes deconvolution on BCDs following the steps outlined by Velusamy et al. (2008). The mosaic and the HiRes images cover an angular size of $5'$ centered on the Cep E protostar. All the HiRes images shown in this paper were obtained after 50 iterations unless mentioned otherwise.

The mosaic and the HiRes deconvolved images in the IRAC and MIPS bands, shown in Figures 1 and 2 respectively, bring out the merits of HiRes processing. In these figures the top panels show the reprocessed HiRes images and the corresponding observed (mosaic) images are shown in the lower panels. The mosaic and HiRes images have identical angular extent and scale. The images are presented using a square-root intensity scale and color stretches. The color stretches used are similar in all images and an example of the colors representing the relative intensities is shown by the wedge at the upper left. In the MIPS 24 μ m mosaic image only the protostar is obvious. However, in the HiRes image at least three additional features along the atomic jet become identifiable

as sources distinct from the “side lobes” present in the mosaic image. These were not identified in previously published mosaic images.

The MIPS images shown in Fig. 2 have small pointing differences ($\sim 1''$) with respect to the IRAC images in Fig. 1. A comparison of the point sources in the MIPS 24 μm image with their counterparts in the IRAC bands indicated that the pointing at 24 μm was off with respect to the IRAC bands by $-0.07''$ in RA and $+1.1''$ in Declination. We shifted the MIPS 70 μm map position by matching the protostar position with the MIPS 24 μm image. In all subsequent displays and analysis we use the MIPS images corrected for their position shifts with respect to the IRAC images.

3. RESULTS AND DISCUSSION

The *Spitzer* IRAC and MIPS bands offer a unique resource to study a wide range of components simultaneously: protostars, protostellar disks, outflows, protostellar envelopes and cores. At the short wavelength IRAC bands the outflow cones are observable in scattered light from the protostar through the cavity created by the jets and outflows (cf. Tobin et al. 2007; Velusamy et al. 2007). A significant fraction of the emission in the IRAC bands is also considered to contain emission from the H_2 rotational lines (e.g. Noriega-Crespo et al. 2004a,b; Neufeld & Yuan, 2008; Smith & Rosen, 2005) and therefore is an excellent tracer of H_2 emission in the protostellar jets. Recently Velusamy et al. (2007) have shown that molecular jets and molecular gas in the bow shocks are readily identifiable in the IRAC bands, while the hottest atomic/ionic gases in the bow shocks, are also identifiable in the MIPS 24 μm band which covers a few atomic/ionic emission lines. The dust emission from the protostar in the MIPS bands is a good diagnostic of the circumstellar disks. Finally, an extended flattened infall envelope perpendicular to the outflow has been seen in the IRAC 8 μm in absorption against the background interstellar PAH emission (Looney et al. 2007; Tobin et al. 2010). *Spitzer*’s coverage of a broad range of IR emissions in the IRAC and MIPS bands with high sensitivity and photometric stability along with the IRS data in some cases, provide sufficient data for a comprehensive modeling of the SED to derive the physical characteristics and the evolutionary stages of protostars (cf. Robitaille et al. 2007; Forbrich et al. 2010). However, by applying the HiRes re-processing we can extract even more information from the *Spitzer* data. The sensitivity, the resolution enhancement and removal of the diffraction lobe confusion have led to visualizing and characterizing more clearly the following features in the Cep E protostar:

1. very high dynamic range maps in which the protostar is well resolved on a sub-arcsec scale from the surrounding jets and outflows
2. wide-angle outflow cavities in the IRAC 3.6 and 4.5 μm images identified by the scattered photospheric starlight; Though they are visible in the Mosaic (standard PostBCD products), they are brought out more clearly in the HiRes images.
3. jets and bow shocks in H_2 molecular emission within the IRAC bands,

4. hottest atomic/ionic gas in the jet head traced by the $[\text{Fe II}]/[\text{S I}]$ line emissions within MIPS 24 μm continuum band.
5. flattened infall envelope around the protostar seen in extinction at 8 μm .

3.1. Protostar

The protostar in Cep E is detected in all IRAC and MIPS bands. The IRAC HiRes images shown in Fig. 1 have high dynamic range, but the brightest features are shown saturated as they are optimized to highlight the low surface brightness emission. In all bands the highest brightness is at the protostar location while the jets and the outflow features are at very low brightness, at levels of $\sim 1\%$ or less of the peak brightness. The color stretch used in Fig. 1 is designed to bring out these low surface brightness features and therefore, underrepresents the peak brightness at the protostar. In Figure 3 we show the HiRes intensity contour maps of the protostar in all bands. To bring out the huge intensity contrast between the brightest emission at the protostar and the weaker emission of the outflow-jet features plotted in Fig. 3, we show selected contours: the lowest level at 0.01% and the highest at 50% of the peak. The observed flux densities and sizes for the protostar are summarized in Table 1. In the IRAC wavelengths the emission from the protostar appears to be unresolved with sizes comparable to the HiRes beam. The protostar flux densities measured in the HiRes maps listed in Table 1 are consistent with the photometric estimates discussed below in section 3.4.

Cep E is believed to be a double source separated by $1.4''$ ($\sim 1000\text{AU}$) as shown by the 222 GHz millimeter interferometric observations of Moro-Martín et al. (2001). However, as seen in Fig. 3, the overlay of mm source positions on the IRAC 3.6 μm map does not show any evidence for a double source in the IR bands. The sub-arcsec resolution ($\sim 0.6'' - 0.8''$) in the HiRes images would have clearly resolved any double source if present. Though the protostar emission is barely resolved in the maps, there is a hint of slight elongation roughly along the separation between the mm-double sources. Our results do not show any evidence for the presence of a second protostellar component. Instead, we suggest that the resolved mm double source structure may represent circumstellar cold dust within a few $\times 10^3$ AU.

3.2. Wide Angle Outflows and Jets: IRAC Images

It can be difficult to observe the extended low surface brightness features associated with the outflow or jets as they may be severely confused by the high brightness of the protostar and the disk. Deconvolution at best removes, or at least minimizes, the diffraction effects of the brightest features, thus enabling improved visualization of the low surface features around them. Furthermore the resolution enhancement provides a sharper view of the outflow cavity walls, molecular jets, and bow shocks.

3.2.1. Wide Angle Outflow Component

The radiation from deeply embedded young protostars is completely opaque at short wavelengths and we can observe only the scattered light escaping along the bipolar cavities produced by their jets and outflows. The

scattering models (cf. Whitney et al. 2003a & b; Tobin et al. 2007) show that such outflow cavities can be traced in *Spitzer* images in IRAC 3.6 and 4.5 μm bands, as is seen more clearly in the HiRes deconvolved images (Velusamy et al. 2007; 2008). In Fig. 1 a wide-angle biconical outflow is clearly detected in the HiRes images at 3.6 and 4.5 μm . Though its presence is marginally evident in the mosaic images, its morphological details are delineated more clearly only in the HiRes images. The wide angle outflow is clearly detected in the light from the protostar scattered by the outflow cavity. Scattered light is brightest at the 3.6 and 4.5 μm bands. As expected for the photospheric light emitted by a protostar at $T \sim 4000\text{K}$ (see section 3.4), the scattered light tracing the wide angle outflow component is relatively weak at 5.8 μm and nearly absent in the 8 μm image. In contrast to this wide angle outflow traced by the scattered light from the protostar, the narrower and collimated jets and the associated bow shocks are detected by their H_2 emission in all the IRAC bands. All the four IRAC bands contain a few H_2 spectral lines (see below for details). While bands 1 and 2 show both the wide angle outflow (in scattered light) and narrow jet features (in H_2 emission), the bands 3 and 4 are dominated by the latter. In the HiRes images the jet emission features show well resolved knots and bow shocks. In the north lobe alone there are at least 16 such features (see Fig. 5a).

The HiRes processing brings out the morphology of the jet and outflow more clearly. In Fig. 4 we show a comparison between the 4.5 μm and 8 μm images by overlaying a schematic of the geometry of the wide angle outflow with its inner boundary matching the outer extent of the jet and bow shocks. The 8 μm emission delineates the narrow jet traced by the entrained H_2 emission, while at 4.5 μm , in addition to the jet, the wide angle outflow cavity is clearly visible. The scattered light seen in the 3.6 μm (Fig. 1) and 4.5 μm (Figs. 1 & 4) delineates a sharp conical boundary for the outflow cavity. The projected opening angle of the cavity is $\sim 85^\circ$ in the 3.6 μm image which is significantly large and places it among those with very wide outflows (Velusamy & Langer 1998; Arce & Sargent 2006) and those with simultaneous presence of high velocity jets (Velusamy et al. 2007; Torrelles et al. 2010 and references therein). The wide angle outflow seen here in the scattered light closely resembles the $^{13}\text{CO}(1-0)$ low velocity lobes (Moro-Martín et al. 2001) with the blue shifted SW lobe approaching the observer. However, the spatial resolution in the CO maps ($8'' \times 7''$) cannot resolve the sharp edges of the wide angle outflow cavity walls as seen more clearly in the scattered light images with sub-arcsec resolution presented here.

Poorly collimated flows can be due to extreme precession of the jet (e.g. Shepherd et al. 2000) and are indistinguishable from the apparent wide angle outflows. In the *Spitzer* image, shown in Fig. 4(a), there is a “second jet/outflow” nearly perpendicular to the main north-south outflow as indicated by the east-west ellipse. The presence of this secondary jet was first observed, earlier in the H_2 2.12 μm image (Eisloffel et al. 1996). The two brightest knots in the 4.5 μm image were clearly detected in their H_2 2.12 μm image while the eastern most knot is outside the 2.12 μm image. In a later H_2 2.12 μm image (Ladd & Hodapp, 1997) all three 4.5 μm knots are detected. The presence of two outflows nearly per-

pendicular to each other suggests the driving source in Cep E is a binary with a separation 4 - 20 AU ($0.005'' - 0.03''$), and disk radius 110 AU (Terquem et al. 1999). A binary systems enhances the effects of precession of both the primary and secondary jets. Eisloffel et al. interpret the wiggles in the loci of the H_2 2.12 μm knots as due to precession with a period of 400 yr and a pitch angle 4° . Binaries with multiple outflows may be common; for example: HH111/HH121 (cf. Gredel & Reipurth, 1993) and L1551 (cf. Rodríguez et al. 1998). Therefore we cannot rule out that the observed wide angle cavity in Cep E is the result of precessing jets. Indeed the combined effect of the precessing jet along with the geometry of the “infall envelope” (discussed in section 3.5) is an alternate scenario as the cause for the observed wide angle cavity. In the absence of direct observational evidence on the outflow motions using high spatial resolution data of CO or other molecular tracers we cannot identify with certainty the wide angle cavity detected in scattered light as wide angle outflow.

In the jet driven outflow models the outflow emission near the protostar may be interpreted as the wings of the bowshocks extending towards the protostar (e.g. Raga et al. 2004). However, in these models the opening angle of the cavities near the protostar tends to be extremely narrow, in contrast to the wide angle observed in Cep E. Furthermore, the emission in the the bow shock is distinctly different, predominantly H_2 emission, as seen in the IRAC images along the jet axis; but in the wide angle outflow region the H_2 emission is totally absent as seen by the high contrast between the emissions in the 4.5 μm and 8 μm bands in Fig. 4. The lack of H_2 emission and the prevalence of scattered photospheric light rule out the possibility that the wide angle outflow is part of the jet driven bow shock. Thus we can constrain the extent of any jet precession to be strictly confined to the emission region in the 8 μm image as shown by the schematic in Fig. 4.

Whatever is the cause for the wide angle cavity in Cep E (by precessing jets or by wide angle low velocity outflow), in *Spitzer* images it is observable only in the scattered light. We can clearly distinguish between the jet and the wide angle cavity by using the IRAC colors for scattered light in the wide angle cavity and H_2 emission in the narrow high velocity jets. In Fig. 4a the 8 μm emission (dominated by H_2 emission in the jets and bow shocks) correlates well with the inner narrow jet features in the 4.5 μm image, but not with the biconical emission away from the jet. Thus it is clear that biconical low surface emission is distinctly different from the jet emission and it is coming from the scattered light in a wide angle cavity. In Fig. 4a the geometry of the wide angle outflow and the narrow high velocity jets in the northern lobe are shown schematically by conical boundaries. The emission in the region outside the inner cone clearly represents the scattered light in the wide angle outflow and that from inside the inner cone boundary represents the jets and their associated bow shocks. To study the spectral characteristics of the scattered photospheric emission from the protostar in the wide angle outflow cavity we were able to separate the scattered emission from the jet emission by computing the flux densities at each IRAC band integrated over the area between the inner and outer boundaries of the out-

flow cone as shown in Fig. 4a. The scattered light flux density spectral plot is shown in Fig. 4b. This spectrum is distinctly different from those in Fig. 6a for the “knots” in the jets and bowshocks. On the other hand, between $4.5\ \mu\text{m}$ and $8\ \mu\text{m}$ it is suggestive of the photospheric (at $T=4300\text{K}$) emission spectrum (shown in Fig. 9) obtained from the SED analysis (see section 3.4), if we take into consideration the effects of higher extinction at $3.6\ \mu\text{m}$. The K-band extinctions are in the range of 2.1 to 2.4 mag across the northern lobe and 1.4 mag for the southern lobe (Smith et al. 2003). The lower flux density at $3.6\ \mu\text{m}$, even after the extinction correction (using the near-IR to mid-IR extinction relations given by Indebetouw et al. 2005; Chapman et al. 2009), would still be consistent with the examples of the SEDs for the scattered light which show a dip near $3\ \mu\text{m}$ due to the scattering albedo (Whitney et al. 2003b). A comparison between the stellar and the scattered light spectra will require detailed modeling including the grain properties and the outflow geometry (Whitney et al. 2003a & b) as presented for the bright scattered light emission from NIR to MIR in the bipolar outflow cavities of the Class 0 object L1527 (Tobin et al. 2008). However, it is possible that, in addition to the complex inner structure generated by the outflow cavities, some of the observed scattered light could result from the outer layers of the extended disk which forms from infalling matter (Tobin, Hartman, & Loinard, 2010).

3.2.2. H_2 Jet Component

Most of the thermal energy associated with the shocks in the outflow is radiated away through the H_2 emission in the rotational transitions; in the L1157 outflow, Nisini et al. (2010) estimate about 50% of the total shock radiated energy is in H_2 emissions. The similarity between the jet/bowshock emissions along the jet axis in all the IRAC images is due to the fact that the mid IR jet emission is dominated by the H_2 pure rotational transitions and each IRAC band contains several of the H_2 lines. (See Neufeld & Yuan (2008) and Ybarra & Lada (2009) for the details on their contributions to the band intensities.) Below we list the H_2 lines in each IRAC band and their upper state energy in degrees K, as a measure of the excitation required for their emission:

3.6 μm : $\text{H}_2\ v = 1 - 0$ O(5)[6952K]; O(6)[7584K]; O(7)[8366K]; $\text{H}_2\ v = 0 - 0$ S(13)[17445K]

4.5 μm : $\text{H}_2\ v = 0 - 0$ S(12)[15542K]; S(11)[13704K]; S(10)[11941K]; S(9) [10362K]

5.8 μm : $\text{H}_2\ v = 0 - 0$ S(8) [8768K]; S(7)[7197K]; S(6) [5830K]

8.0 μm : $\text{H}_2\ v = 0 - 0$ S(5) [4587K]; S(4)[3475K]

To demonstrate how these H_2 lines could be used to study the outflows, Smith & Rosen (2005) show examples of synthetic images of H_2 emission in each IRAC band using model images obtained in hydrodynamical simulations of dense supersonic molecular jets. In addition to the lines listed above, Smith & Rosen (2005) include in each IRAC band a few other $\text{H}_2\ v = 1 - 1$ and $\text{H}_2\ v = 2 - 1$ transitions. The $3.6\ \mu\text{m}$ band is dominated by emission from vibrationally excited H_2 lines with higher mean excitation energies, while the other bands are dominated by rotational lines.

The H_2 emission in a few selected outflows have been well studied using the H_2 pure rotational lines from S(0)

to S(7) with IRS mapping (e.g. Neufeld et al. 2006; Nisini et al. 2010). No IRS mapping data is available for Cep E, however, Noriega-Crespo et al. (2004b) used the H_2 rotational transition lines in the IRS spectrum at a single pointing near the brightest emission in the northern lobe (see Fig. 6) to estimate the mean excitation temperature (686 K) and a number density ($6 \times 10^4\ \text{cm}^{-3}$). Moro-Martín et al. (2001) used the pure rotational $\text{H}_2\ 0-0$ lines S(2) to S(7) intensities in 7 discrete positions observed by ISOCAM CVF and their excitation diagrams, to model the temperatures and densities in the bowshocks. The mid-IR H_2 emission is interpreted in terms of shocks produced by the high velocity atomic/ionic jets. High-density C-shock models can best account for the brightness of the H_2 emission (Smith et al. 2003; Dionatos et al. 2010). In Cep E by comparison with C-type shock models, the H_2 line ratios observed in the IRS spectrum give a mean shock velocity of $20\ \text{km s}^{-1}$ (Noriega-Crespo et al. 2004b). Since the intensities of the H_2 lines within each IRAC band are sensitive to a wide range of excitation conditions, the relative intensities in each band can be used as a diagnostic of the physical conditions in the shocks. As demonstrated by Ybarra & Lada (2009) we can therefore, use the IRAC colors: $[3.6] - [4.5]$ versus $[4.5] - [5.8]$, to study the shocked H_2 at sufficiently high temperature ($2000\text{K} - 4000\text{K}$) and neutral atomic hydrogen density ($10^3 - 10^4\ \text{cm}^{-3}$) in jets/outflows.

The $8\ \mu\text{m}$ image clearly delineates the outer boundary of the jets and their associated bowshock emissions as shown by the schematic in Fig. 4. In all IRAC bands within this region a number of jet features with resolved bowshock structures are identified along both north and south lobes. Near-IR high resolution $\text{H}_2\ 1-0$ S(1) imaging has shown that the lobes consist of numerous emission knots (Eisloffel et al. 1996; Ladd & Hodapp, 1997). Smith et al. (2003) estimate about 20 bow shocks, close to paraboloidal in shape, are required by the model to explain the integrated emission for each lobe. As indicated in the left panels in Figs. 5a & 5b, in the IRAC $8\ \mu\text{m}$ image we identify at least 22 such resolved jet/bowshock components. As seen in Fig. 1 the emissions in both lobes along the jet axis in all four IRAC bands appear to be morphologically very similar. Although all the knots identified at $8\ \mu\text{m}$ (Fig. 5) have counterparts in all other bands, their relative intensities vary widely. Furthermore, in the $4.5\ \mu\text{m}$ image we could easily identify at least an additional seven knots (indicated as A1 to A7 in Fig.5) which appear less prominently at $8\ \mu\text{m}$. To characterize fully the shock conditions in these H_2 knots and bowshock features and to bring out their differences, we constructed the IRAC channel difference images (Figure 5): $4.5\ \mu\text{m} - 3.6\ \mu\text{m}$, $5.8\ \mu\text{m} - 4.5\ \mu\text{m}$, and $8\ \mu\text{m} - 4.5\ \mu\text{m}$. The difference image $4.5\ \mu\text{m} - 3.6\ \mu\text{m}$ is more like a continuum subtracted H_2 line emission (assuming the $3.6\ \mu\text{m}$ band behaves like a continuum filter with little H_2 line emission) and resembles the $2.12\ \mu\text{m}$ image (Eisloffel et al. 1996; Ladd & Hodapp, 1997), tracing the brightest emission closer to the leading bowshock edges on small scales, while the difference images, $5.8\ \mu\text{m} - 4.5\ \mu\text{m}$ and $8\ \mu\text{m} - 4.5\ \mu\text{m}$, show strong color differences determined by the shock excitation along the wings, spatially away from their leading edges.

To obtain a more quantitative description of the knots identified in Fig. 5 we measured their flux densities in each IRAC band by integrating over a $1.5'' \times 1.5''$ area and these are also shown as spectral plots in Fig. 6a. Though the images have sub-arcsec resolution, to obtain a more robust estimation of the flux densities we used a larger area of integration. These spectra indicate that the excitation conditions vary widely among the knots: fourteen (including all seven selected by the $4.5 \mu\text{m}$ peak emission) have apparent spectral peaks at $4.5 \mu\text{m}$; ten have spectral peaks between 5.8 and $8 \mu\text{m}$, while five have no apparent peak with fluxes increasing beyond $8 \mu\text{m}$. These differences are also clearly brought out in the difference images shown in Fig. 5. The extinction corrections will increase the fluxes at 3.6 and 4.5 microns relative to the others; however, the spectral shapes do not change significantly. Our results of such strong $4.5 \mu\text{m}$ emission is consistent with the hydrodynamic simulations of Smith & Rosen (2005). The knots with the highest excitation as inferred from the narrow spectral peaks at $4.5 \mu\text{m}$ (nos. K7, K6 and K2) are all located near the brightest tips of the southern and northern lobes respectively. While the knots K7 and K6 are among the brightest, the knot K2 is only marginally bright. Except for these three, there is no other striking correlation between the excitation conditions (spectral peak/shape) in the knots and their radial distance from the protostar or any particular age sequence.

The IRAC H_2 emission spectral data presented here will be useful to constrain the C-shock models for each jet feature along with those available in the near IR. We use the colors $[3.6] - [4.5]$ and $[4.5] - [5.8]$ derived from the spectral data for each knot as diagnostics to constrain the temperature and densities as discussed by Ybarra & Lada (2009). The IRAC color-color plot for the H_2 knots in Cep E is shown in Fig. 6b. The labels in Fig. 6b represent the color-color regime for each H_2 knot, identified in Fig. 5. The IRAC color-color plot for Cep E knots is remarkably similar to those obtained for HH54 (Ybarra & Lada, 2009). The majority of the knots, 17 out of 29, appear to have excitation conditions corresponding to temperatures 2500K to 4000K and densities 10^3 to 10^4 cm^{-3} .

The observed bowshock structures (leading edges and wings) projected on the sky and the subsequent interpretation of their shock layers emitting in different IRAC bands is critically dependent on the observer's viewing geometry with respect to the shock. Taking advantage of the sub-arcsec resolution in the deconvolved IRAC images we can study in some greater detail the spatial characteristics in each image to resolve shock geometry. In Fig. 7 we show a blowup of the IRAC images near the tip of the NE and SW lobes. We use the geometrical shape of the $4.5 \mu\text{m}$ and $8 \mu\text{m}$ emissions of the shock features combined with their relative displacements to "infer" the direction the shocks which is likely to be consistent with the schematic bowshock structure, for example as shown in Fig. 13 in Moro-Martín et al. (2001). In such cases we expect the atomic/ionic emission lines to originate at the tip of the bowshock (in the "Mach disk" and stagnation tip) where the J- shocks are dominant. But, the H_2 line emissions originate farther down along the bowshock wings where the shocks are oblique and more likely to be C-type. For a better understanding of the relationship

between the structural complexity in the IRAC emissions and their colors with the atomic/ionic jet head, we plot in Figs. 7a & 7b the atomic jet traced by the MIPS $24 \mu\text{m}$ emission from the $[\text{Fe II}]$ and $[\text{S I}]$ lines (discussed below in section 3.3). The $24 \mu\text{m}$ emission contour defines the location of the jet head (Mach disk/stagnation tip) which is driving the bowshock. The high excitation H_2 lines in the $4.5 \mu\text{m}$ band are likely to be relatively closer to the "tip" than the low excitation traced by $8 \mu\text{m}$ band. Schematically, in Figs. 7a & 7b the $4.5 \mu\text{m}$ intensity contours overlaid on the $8 \mu\text{m}$ grey scale delineate the bowshock closer to its leading edge (the tip) while the $8 \mu\text{m}$ emission traces the projected spatial structure the bowshock wings away from the tip. The bright and dark bands seen across several knots in the $5.8 \mu\text{m} - 4.5 \mu\text{m}$ and $8 \mu\text{m} - 4.5 \mu\text{m}$ difference images (eg. nos. 9, 10, 12, K4, K7, 21 in the right two panels in Figs. 5a & 5b) trace the projected separation between the bowshock tips and wings. The geometry in two systems of knots consisting of nos. 3/5/6 (Fig. 5a and 7a) and K5/18/19 (Fig. 5b) respectively, seems consistent with each one describing a bowshock tip with wings on either side, moving nearly in the plane of the sky. The two outermost arc-like emission features in the $4.5 \mu\text{m}$ emission (Fig. 7a) are also detected at $2.12 \mu\text{m}$ (Ladd & Hodapp, 1997). However, the outermost arc-like emission at $8 \mu\text{m}$ (Fig. 7a) is located between the two $4.5 \mu\text{m}$ arcs, behind the leading outer $4.5 \mu\text{m}$ arc and slightly ahead of the second $4.5 \mu\text{m}$ arc, with $\sim 1.5''$ (1000 AU) separation between them. The $8 \mu\text{m}$ arc does not seem consistent with bowshock wings but rather with a shocked layer between two successive leading shocks described by the $4.5 \mu\text{m}$ and $2.12 \mu\text{m}$ arcs and originating in two successive ejections. It is interesting to note that the $4.5 \mu\text{m}$ outermost arc has a flux density spectrum (K1 in Fig. 6a) resembling that of the scattered light in the wide angle outflow cavity (Fig. 4b). It is, therefore, possible that this outermost arc indeed represents scattered light in the cavity produced by the NE jet. However, the continuum subtracted $2.12 \mu\text{m}$ H_2 line emission (Ladd & Hodapp, 1997) strongly favors its identifications as a bowshock H_2 emission feature.

The IRAC data for emissions near the SW tip as shown in Figs. 5b and 7b suggest a very complex system of oblique (C-type) shocks with possible twists in the jet kinematics and geometry. The cartoon in Fig. 7b shows a plausible scenario for the C-type shocks, seen in projection, as traced by IRAC bands. The location of the jet head (Mach disk/stagnation tip) which is driving the bowshock is indicated by the $24 \mu\text{m}$ emission contours. The multiple C-type shocks suggested by the $4.5 \mu\text{m}$ and $8 \mu\text{m}$ emissions, surrounding the $24 \mu\text{m}$ jet feature, seem to be tracing different pieces of the bowshock and its wings, expanding into or out of the plane (but seen in projection on the sky), all driven by a single jet-head. In Fig. 7b the long arrow marks the general direction of the atomic jet while the short arrows indicate oblique shocks moving in and out of the plane. We can interpret the relative outward and inward displacements of the $4.5 \mu\text{m}$ emissions with respect to the $8 \mu\text{m}$ for knots K7 and 21, respectively, as due to the viewing geometry of the observer and the C-type shock orientations. As another example of the geometry of the bowshock with respect to the Mach disk, in Fig. 7a we show the association between the $24 \mu\text{m}$ atomic/ionic jet feature (#2

in Fig. 8a)) and the bowshock traced by knots 4, 5 and 6 (identified as arc no.3 in Fig. 7a).

3.3. Atomic Jets: MIPS 24 μm Compact Sources

In Fig. 8 we show an overlay of the MIPS 24 μm HiRes image (as contours) on the 4.5 μm image. At 24 μm , in addition to the protostar, we detect at least three compact features coincident with the brightest emission in the bow shocks as traced by the H_2 emission in the 4.5 μm and other IRAC bands. These compact emissions at MIPS 24 μm coincide with the jet heads. Although some enhanced emission from the collisionally heated dust in the shocks is possible, it is more likely that the 24 μm emission is tracing the hottest atomic/ionic gas in the bow shocks, possibly similar to that seen in the HH46/47 system (Velusamy et al. 2007). In contrast to the morphology of the H_2 emission, which are bow shocks with extended long arcs, the 24 μm emission is more compact and is confined to the tip of the bow shock coinciding with the jet head. We can expect to see such differences if the 24 μm emission is produced by higher excitation (velocity) shocks arising closer to the apex of the jet as in the case of J-shocks, while the H_2 emission is produced further back in the low velocity C-shocks. We can, therefore, interpret the 24 μm emission to represent that produced in the J-shocks (ionic/atomic shocks) from the bright [Fe II] line emissions at 24.51 and 25.98 μm within the MIPS pass band, as observed in the case of HH46/47. For one of the sources, #1 in Fig. 8a, we can use the IRS spectral data to substantiate the fact that the 24 μm emission is indeed atomic. In the previously published IRS spectrum (Fig. 6 in Noriega-Crespo et al. 2004b) of this feature we identify only the [S I] $^3P_1 - ^3P_2$ line at 24.249 μm , but no [Fe II] line emissions. In order to characterize the atomic emissions within the MIPS 24 μm pass band, we replotted the spectrum using the IRS data obtained from the *Spitzer* Archives. This spectrum, shown in Fig. 8b, is consistent with the published spectrum except for the baseline subtraction. The [S I] line first detected by Noriega-Crespo et al. (2004b) in this position in Cep E is clearly seen in this spectrum. The [Fe II] line at 25.98 μm and the H_2 S(0) at 28.22 μm are also detected with relatively low intensities. We use the intensities in this spectrum ([S I] at 0.82 Jy and [Fe II] at 0.06 Jy) to estimate qualitatively the contribution to the 24 μm pass band from the atomic spectral lines within the MIPS pass band as indicated in Fig. 6b. The total integrated line emission corresponds to 0.64 Jy in a single IRS channel (0.17 μm wide which is about 3% of the total pass band) appearing at $\sim 60\%$ level of the pass band response. We would then expect this line emission to appear as a 13 mJy continuum source in the MIPS 24 μm image. Thus, in the HiRes image (with 2'' spatial resolution) we expect it to have a brightness of ~ 136 MJy sr^{-1} . This value is in reasonable agreement with the observed brightness of 103 MJy sr^{-1} , considering the uncertainties in estimating the equivalent intensity in the MIPS continuum band for a given channel intensity in the IRS spectrum. We therefore conclude that the 24 μm emission in this jet feature in Cep E is truly atomic in origin, primarily from [S I]. Thus after HiRes reprocessing, the *Spitzer* MIPS 24 μm image is found to be an extremely useful diagnostic of the atomic component of

the protostellar jets.

For the other two 24 μm sources (#2 and #3 as marked by the short arrows in Fig. 8a) seen along the jet emission, there are no matching IRS spectra to interpret the origin of their emission as atomic/ionic gas in the jet heads. However in the case of #3 strong [S II] $\lambda\lambda 6717/31$ emission is observed by Ayala et al. (2000) in this position which coincides with HH 377. - Furthermore, [S II] and [Fe II] have very similar excitation energies (Nisini et al. 2002) and therefore, we can expect a significant contribution from [S I] and/or [Fe II] to the MIPS 24 μm emission. Their location along the jet axis coincides well with the bright emission knots/jet heads (inferred as arising from H_2) seen in the IRAC bands. Also their positions coincide with the tip of the bow shocks. We expect to see [S I] and [Fe II] fine structure line emission in the spectra of HH objects, which show the classical signatures of collisional excitation similar to those observed in the IRS spectra of supernova remnants like IC 443 (Noriega-Crespo et al. 2009). Therefore, by analogy to that identified in the jets of HH46/47 system (Velusamy et al. 2007), we can regard these 24 μm emission features to have the same characteristics as the source #1 discussed above. Among the three, the source #3 in the south lobe is the brightest (peak at 345 MJy sr^{-1}) which is also the brightest emission in the IRAC bands. The second brightest source #2 (with peak 145 MJy sr^{-1}) is located in the NE lobe, farther away than source #1, but the IRAC emission here is weaker than for source #1. In the close vicinity of the sources #1 and #2 there are multiple bow shocks and jet heads in the IRAC bands. However the 24 μm peaks are exclusively coincident with only one of the jet heads implying that not all bow shocks and jet heads have associated 24 μm sources. In other words, not all jet heads have detectable atomic/ionic emission. The two outermost bow shocks in the northern lobe, which are clearly seen in the IRAC bands (see Fig. 7a), do not show any compact 24 μm sources. Furthermore, these bow shocks do not show the bright jet heads as seen in the other cases.

As pointed out earlier, not all jet heads or knots with strong H_2 emission in the IRAC bands have associated atomic/ionic counterparts. The atomic/ionic emission appears to require higher excitation shocks than those producing the mid-IR H_2 lines. Dionatos et al. (2010) discuss in detail the physical conditions required for the mid-IR atomic/ionic and H_2 line emissions in these jet features. They show that the low velocity 10 - 15 km s^{-1} shock models that best fit the warm H_2 emission are unable to reproduce the observed [Fe II] in HH211. It would be difficult for us to quantify the differences in H_2 and atomic/ionic emission from the jet heads or knots in Cep E without appropriate shock models. However, the association between the 24 μm atomic/ionic jet feature and the bow shock knots observed in IRAC bands can be interpreted in terms of the schematic bowshock model as discussed above in section 3.2.2. The 24 μm feature #3 is associated with several knots K6, K7, 21 and 22 (in Fig. 5b and Fig. 7b) and it can be identified as the Mach disk driving a system of oblique C-type shocks represented by these knots. Similarly, the 24 μm compact source #1 is associated with the 4.5 & 8 μm knots no. 10, K3 and K4 respectively (Fig. 5a) and can be interpreted as the

atomic/ionic jet driving the bow shock represented by these knots around it. The 24 μm atomic/ionic jet feature #2 brings out even more clearly its association with the bow shock and its wings observed in IRAC bands. This feature is associated with the knots 4, 5 & 6, and the diffuse emission along the bowshock wings (arc no. 3 as shown in Fig. 7a).

So far, we have IRS spectral data for only two 24 μm compact sources associated with the atomic jet head (knots), but they seem to have very different atomic spectral characteristics. The jet head in the HH46/47 system shows a strong [Fe II] line while that in Cep E shows a strong [S I] line and very weak [Fe II]. Such differences suggest that the physical conditions in the jet heads or knots can vary widely. The IRS spectral line intensities in the jet heads or knots, similar to those in Cep E and HH46/47, in HH211 (Dionatos et al. 2010), HH54, HH 7-11 (Neufeld et al. 2006), BHR71, L1157, L1448, NGC 2071, and VLA 1623 (Neufeld et al. 2009), show a wide variation in the intensity ratio [Fe II]26 μm to [S I]25 μm . Such variations can be interpreted as electron density and temperature effects on the ionization of Fe, as well as differences in the collisional excitation. Neufeld et al. (2009) find evidence for some spatial segregation between the [S I] and [Fe II] emitting regions, suggesting that [Fe II] is tracing the faster, dissociative shocks. Thus the differences between the 24 μm features in Cep E and HH46/47 are due to their shock conditions, namely shocks in Cep E being less dissociative than in HH46/47.

The ISO-LWS spectra of both the north and south lobes in Cep E detected strong [O I] 63 μm and [C II] 158 μm emissions (Moro-Martín et al. 2001), which are the most efficient coolants in low velocity dissociative shocks. The low intensity features in the deconvolved MIPS 70 μm image (Fig. 2) are very intriguing, especially since they lie along the jet/outflow lobes in Cep E. Of special interest to us is the fact that the MIPS 70 μm band includes the [O I] 63 μm line near the end of its passband at $\sim 75\%$ response. In the ISO LWS spectra the [O I] 63 μm line was detected as the brightest line emission with intensities of 9.3 and 12×10^{-19} W cm^{-2} at the NE and SW lobes respectively. Such emission would be observed in the MIPS 70 μm image as continuum sources with total flux densities of 0.58 Jy and 0.75 Jy respectively for the NE and SW lobes which are higher by a factor 2 to 3 than the features in Fig. 2. These feature are at intensities at a level of 0.1% of the peak (protostar) emission. The SW feature is the brighter of the two and in the 70 μm Point Response Function (PRF) it coincides with an enhanced sidelobe in the Airy ring, at $\sim 6.3\%$ level. We believe the MIPS 70 μm data does not warrant such high dynamic range (> 1000) in the HiRes processed image. These features appear to be residuals of the Airy ring. Furthermore, their locations do not seem to correlate with any of the features observed in 24 μm or the IRAC bands.

3.4. Photometric SED Analysis of Cep E Protostellar Emission

We obtained the *Spitzer* IRAC and MIPS photometry using the mosaic images. For the IRAC data we used the artifact corrected BCD's (cbcd images) and Imasks (bimask), with the standard overlap and mosaic modules, to create the mosaic images for each of the IRAC bands.

The mosaics were done using a pixratio=2, which results in a pixel scale of 0.6'' per mosaic pixel. IRAC photometry was obtained by using the PHOT task in IRAF. An aperture radius of 4 pixels (2.4''), sky annulus between 4 and 8 pixels, was used to obtain the aperture photometry. For the 3.6 μm , 4.5 μm , 5.8 μm and 8 μm bands we used zero point magnitudes of 18.59, 18.09, 17.48 and 16.7 respectively, and corresponding aperture corrections of 1.213, 1.234, 1.379 and 1.584.

The *Spitzer* MIPS BCD data in the 24 μm and 70 μm bands were used to create the basic mosaics using the relevant templates in the MOPEX software. Subsequently, photometry was obtained by using the appropriate default MOPEX/APEX single-frame templates for each band. The recommendations of the *Spitzer* data analysis cookbook recipe 24 were followed.³ We note that our MIPS photometry agrees with the photometry derived by Noriega-Crespo et al. (2004b) to better than 5%.

We constructed the spectral energy distribution of the Cep E protostar by combining our *Spitzer* photometry with other photometry from the literature. Chini et al. (2001) have studied this protostar at millimeter wavelengths, using the fluxes at 450 and 850 μm obtained with SCUBA on the JCMT and at 1300 μm with the IRAM telescope. The aperture sizes used to derive the fluxes are all larger than 10'', which is larger than the aperture used to obtain the MIPS 70 μm photometry. In order to model the protostar using the SED fitting tool by Robitaille et al. (2007), it is essential to classify the available data as "data points" and "upper limits". The data points are used to obtain the best model fitting and computing the χ^2 factor, whereas the upper limits serve in constraining the fits. We note that the protostar appears as a point source in the *Spitzer*-IRAC and MIPS bands (Fig. 3). Therefore, we use the IRAC and MIPS photometry as data points in subsequent modeling. The millimeter fluxes from Chini et al. (2001) are obtained from apertures larger than 10'' and could be contaminated by the outflow and surrounding cloud. Therefore, we use the millimeter data points as upper limits. We also use the IRAS 12 μm flux (obtained from an aperture of 30'') as an upper limit. The protostar is not detected in the 2MASS K band, therefore, an upper limit of 16 mag in the K band was used to constrain the SED.

The SED, characterized by these data points and upper limits, is modeled using the SED fitting tool (Robitaille et al. 2007). We note that the actual photometry has an accuracy closer to 1%-2%. However, we assumed photometric uncertainties of 10% as a conservative limit to minimize the risk of including biases in the modeling. The SED fitting tool requires a range of values for the distance and interstellar extinction to the source, in order to scale the models in the grid to the observed data. The lower and upper limits to the distance were set at 0.65 and 0.8 kpc, respectively. The interstellar extinction was set to vary between 2 and 8 visual magnitudes.

The observed SED is well represented by a YSO model in the Class 0/I evolutionary stage. Fig. 7 shows the models fitted to the SED. The detailed physical parameters of the young stellar object system derived from the SED fitting are listed in Table 2. The errors quoted in

³ (<http://ssc.spitzer.caltech.edu/dataanalysis/cookbook/29/>)

Table 2 correspond to the spread in the parameters of the models shown using the grey lines in Fig. 7. Which physical parameters are most reliable depends on what kind of model best describes the observed SED. This philosophy is different from other interpretations of YSO's based on colors or spectral indices alone (for details see: Smith et al. 2010; Gramajo et al. 2010). In a Class 0/I YSO model, it is the envelope properties, listed in Table 3, that are better constrained, in contrast to the disk properties, because the disk is deeply buried inside the envelope. The envelope mass for the Cep E protostar is $\sim 7M_{\odot}$, with an accretion rate of $\sim 10^{-4}M_{\odot} \text{ yr}^{-1}$. The accreting photosphere embedded inside this envelope is currently estimated to have a mass of $\sim 3M_{\odot}$ and a disk mass $\sim 10^{-2}M_{\odot}$. Together, these values support the conjecture that Cep E will become an intermediate mass star of $\sim 4M_{\odot}$ (Froebich et al. 2003; Froebich, 2005) at the end of star formation. The wide angle flow detected in this work may well be the signature of rapid accretion and radiation driven wind from the envelope, which is more appropriate for intermediate mass stars than low mass stars. The inclination angle of the source, obtained by model fitting, is $\sim 42^{\circ} \pm 17^{\circ}$. Our model fitted value agrees, within the uncertainties, with the inclination of $57^{\circ} \pm 7^{\circ}$ derived from the radial velocity and proper motion (Smith et al. 2003).

3.5. Infall Envelope as an IR Absorption Band

Our SED analysis show the existence of an arcmin size dense envelope with $7M_{\odot}$ and size 20,000AU (see Table 3). Such large scale protostellar infall envelopes perpendicular to the outflow are common in Class 0 protostars (cf. Velusamy & Langer 1998; Chang et al. 2010). In the Class 0 protostar L1157, also located in the Cepheus flare, an extended $\sim 2'$ flattened envelope perpendicular to the outflow was seen in the IRAC band at $8 \mu\text{m}$ in absorption against the background interstellar PAH emission (Looney et al. 2007; Tobin et al. 2010). Stutz et al. (2008) detected a similar extinction feature (which they refer to as a shadow) around the protostar in the IRAC $8 \mu\text{m}$ image of B335 consistent with the flattened molecular core. In Fig. 8 we show the mosaic images at $3.6 \mu\text{m}$ and $8 \mu\text{m}$ of a larger region than shown in Fig. 1. To the south of Cep E we can see a large interstellar emission cloud possibly rich in PAH emission, since it is not seen in the $3.6 \mu\text{m}$ image shown for comparison in Fig. 8. To the north of this cloud emission, on both sides, to the east and the west of the Cep E jet/outflow region, we see patches of $8 \mu\text{m}$ absorption of this PAH background. Two patches (indicated by the arrows in Fig. 8b) are seen on either side closest to the protostar. It seems likely that these are the ends of a continuous absorption band which is masked in the middle by the protostar and its bright "side lobes" (Airy rings) around it. It is possible that these absorption features are similar to those seen in L1157 by Looney et al. (2007) but is seen less clearly here because of the confusion by the emission in the sidelobes of the protostar.

Though the HiRes deconvolved image (Fig. 1) is free from the sidelobe contamination from bright sources in the image, we cannot use it for tracing the absorption feature. The HiRes processed images do not contain the background emission to trace this absorption features. Optimal performance HiRes requires that the

background emission is fully subtracted out in each BCD prior to applying the deconvolution. Furthermore, the positivity criteria implicit in the deconvolution algorithm makes it insensitive to negative intensities. However we can still use the HiRes deconvolution on the BCDs with the full background emission present and remove the sidelobes, but sacrificing the full resolution enhancement. For this purpose we stop the HiRes processing with fewer than 10 iterations instead of 50 iterations used for optimal processing. In Fig 8c we show the results of HiRes deconvolution after 10 iterations on the data with the background present. After the removal of the sidelobes the protostellar envelope is traced more clearly by the $8 \mu\text{m}$ absorption extending closer to the protostar. We interpret this absorption feature as the extended protostellar envelope. We estimate an angular size of about $35''$, corresponding to 22,000 AU which is in good agreement with that inferred from the SED analysis. It is most likely that this absorption feature is the infall envelope which is feeding the disk and the forming star in Cep E. Indeed, Gregersen et al. (2000) have detected the infall signature in Cep E using the velocity asymmetries observed in $\text{HCO}^+(3-2)$ with a $26''$ beam. A scenario with an extended infall region is particularly interesting in view of the simultaneous presence of collimated jets and wide angle outflow in Cep E. In the recent models by Machida et al. (2008) the high velocity jets and the low velocity wide angle outflow are driven by two different components, namely, the accretion in the compact protostellar disk driving the jets and the accretion from the extended infall envelope driving the wide angle outflow. Thus, along with the other examples of B335 and L1157, we show that the $8 \mu\text{m}$ extinction is a useful diagnostic of the protostellar envelopes.

3.6. Simultaneous Jets and Wide Angle Outflows

In some protostellar objects both wide angle outflows and collimated jets are seen, while in others only one is observed. These observations raise a number of important questions about jets and outflows, which directly impact our understanding of their role in star and disk formation. What is the origin of the wide-angle outflows and collimated jets and how do they evolve with time? To date, jets and outflows from a protostar have various morphological and kinematical properties such that they cannot be explained by a single-class model. The centrifugal force originates from the rotation of the circumstellar accretion disk and the jets are ultimately powered by the infall of material, with the rotation and magnetic fields playing a crucial role. The magnetocentrifugal origin of jets and their launch from the magnetized accretion disk of the protostar (cf. Ouyed & Pudritz 1997) are generally accepted, although the detailed mechanism is under debate. The wide-angle outflow may also be jet driven (cf. Raga & Cabrit 1993, Ostriker et al. 2001) or wind driven (cf. Shu et al. 2000). In the jet-driven bow shock model, an episodic variation in jet velocity produces an internal bow shock driving an internal shell, in addition to the terminal shock. Poorly collimated flows seen as wide angle outflows can be due to extreme precession of the jet (Shepherd et al. 2000) and indistinguishable from wind driven wide angle outflows. Other explanations include a turbulent jet model (cf. Cantó & Raga 1991; Watson et al. 2004), and a

circulation model, involving radiation and magnetocentrifugal acceleration and collimation producing heated pressure-driven outflows (cf. Lery 2003, Combet et al. 2006).

In a unified model for bipolar jets and outflows Shang et al. (2006) incorporate the essential features of the primary X-wind, which is driven magnetocentrifugally from close to the protostar in the interface between its magnetosphere and the associated circumstellar disk. This primary wind has an angle-dependent density distribution, with a dense axial jet surrounded by a more tenuous wide-angle wind. The resulting structure shows two prominent dense features: a shell of mostly swept-up ambient material and a jet along the axis that is the densest part of the primary wind. The shell can be either well-collimated, as observed for the class of jet-like molecular outflows, or wide open, as in the classical molecular outflows. The morphology of jets and outflow is shaped to a large extent by the ambient mass distribution in the collapsing envelope and thus jet-like and wide angle outflows are unified only in an evolutionary sequence. In the disk-wind model simulations of collapsing, rotating, magnetized Bonnor-Ebert spheres of molecular cores, the highly collimated wind is driven magnetocentrifugally from a wide range of circumstellar disk radii, surrounded by a wide-angle wind driven by toroidal magnetic pressure (e.g. Banerjee & Pudritz 2006). In another unified model Machida et al. (2008) explain the simultaneous occurrences of both the jets and wide angle outflows using the results from their calculation of cloud evolution from a molecular cloud core to a stellar core, starting with a Bonnor-Ebert isothermal core rotating in a uniform magnetic field. They find two distinct flows, wide angle low velocity and narrow high-velocity flows driven by two different components: the collapsing core and the protostar, respectively. These two distinct flows have different degrees of collimation and velocities: the low-velocity flow (i.e. molecular outflow) has a wide opening angle, while the high-velocity flow (i.e., optical jet) has a well-collimated structure. This collimation is caused by both the configuration of the magnetic field lines around the drivers and their driving mechanisms. The low velocity wide-angle outflow, mainly driven by the magnetocentrifugal wind mechanism (disk wind), and guided by hourglass-like field lines; and the fast highly-collimated outflow driven by magnetic pressure and guided by straight field lines near the protostar.

The results of the unified model by Machida et al. (2008), as seen in their schematic (Fig. 15 in their paper), are remarkably similar to the simultaneously present narrow jet and wide angle outflow in Cep E we derive from *Spitzer* observations. This model also appears to be viable for the jet/outflow seen in several other objects such as in B5-IRS1 in which the wide-angle CO outflow (Velusamy and Langer 1998), and the pc scale HH flows (Yu et al. 1999) are likely be driven by the extended infall and the compact disk, respectively. HH46/HH47 (Velusamy et al. 2007), CepA (Torrelles et al. 2011), and HH 211 (Hirano et al. 2006) are a few other examples of simultaneous jets and wide angle outflows in protostars. In outflows of L1448-mm and IRAS 04166+2706, Tafalla et al. (2010) observe evidence for the simultaneous presence of multiple components consisting of a wide angle

slow wind (identified by the line-wings) and collimated flows (identified by the extremely high velocity (EHV) component). A high angular resolution CO(J = 2-1) map of the EHV component in I04166 is well explained as resulting from a series of internal working surfaces traveling along a collimated jet (Santiago-Garca et al. 2009). The large scale morphologies observed in these objects are broadly consistent with any of the above models for the multiple jet/outflow components. Observations with much higher spatial resolution with sufficient sensitivities will be needed to probe the launching region of the primary winds on a scale of a few AU of the protostar to discriminate between various models of jets and outflows. Furthermore a large sample of fully mapped jets and outflows will lead to a better understanding of the simultaneously present jets and wide angle outflow sources in the context of the evolutionary sequences of protostars.

4. CONCLUSIONS

By combining the high sensitivity in the *Spitzer* images and the reprocessing with HiRes we find new jet and outflow features in Cep E in addition to those previously known; the new results are: (i) wide angle outflow seen in the scattered light; (ii) morphological details of at least 29 jet driven bow shocks and jet heads or knots; (iii) three compact features in 24 μm continuum image identified as atomic/ionic line emission coincident with the jet heads; (iv) a flattened arcmin size protostellar envelope seen against the interstellar background PAH emission as an absorption band seen across the protostar at 8 μm . We demonstrate that by separating the protostellar photospheric scattered emission in the wide angle cavity from the jet emission, we can study directly the scattered light spectrum. The simultaneous presence of collimated jets and wide angle outflow in Cep E, as shown here, is consistent with unified jet-outflow models such as by Machida et al. (2008) in which the accretion in the compact protostellar disk drives the high velocity jets and the accretion from the extended infall envelope drives the wide angle outflows. We have obtained the H₂ emission line spectra as observed in all IRAC bands for all 29 knots and use their IRAC colors as probes of the temperature and density in the jets and bowshocks. These spectra are useful as diagnostics of the C-type shock excitation of pure rotational transitions of H₂ and a few H₂ vibrational emissions. A shock excitation model template of IRAC intensity spectra taking into account all H₂ transitions and the spectral response of each IRAC band will be a useful resource for interpreting the vast *Spitzer* data base available to study protostellar jets and outflows. Detailed modeling of the individual shocks will help retrace the history of episodic jet activity and the associated accretion on to the protostar.

Our results for Cep E, which utilize the HiRes algorithm, show the potential of *Spitzer* data to study the entrained molecular H₂ in the high velocity jets as well as the wide angle outflow cavities associated with the slower winds often traced by CO. Our approach for Cep E builds on the earlier work of Velusamy et al. (2007), who identified simultaneous jets and wide angle outflows in the young protostar HH46/HH47. In addition to the *Spitzer* data, the recent mm and sub-mm spectral line observations of outflows and jets from ground (e.g. Tafalla et al. 2010; Santiago-Garca et al. 2009) and from *Herschel*

(e.g. Codella et al. 2010; Lefloch et al. 2010), will offer new clues to the nature of the EHV gas and its relation to the low velocity outflow shells. Though a few selected outflows have been well studied in H_2 emission using all H_2 pure rotational lines from S(0) to S(7) with IRS (e.g. Neufeld et al. 2006; Nisini et al. 2010) the IRAC images available in the *Spitzer* archives have the potential to study the H_2 emission in a large sample of outflow sources. Quantitative analysis of IRAC colors using statistical equilibrium estimates such as those of Ybarra and Lada (2009), demonstrate the value of *Spitzer* images to probe the thermal structure of the shocked gas without the need of using spectroscopic data. Thus, the *Spitzer* capability to study these features in H_2 and scattered light, as described here, will be complementary to the mm/sub-mm molecular data, thus leading to a better understanding of the origin of the atomic jets and the fast and slow molecular outflows, and their subsequent manifestation in the physical and chemical characteristics as observed in the resulting shocks. The *Spitzer* H_2 molecular outflow data is even more relevant now, in the light of recent observations (cf. Tafalla et al. 2010) of the EHV component (in addition to the wing components) in a suite of complex molecules such as CO, SiO, SO, CS, HC_3N , HCO^+ , H_2CO , HCN, H_2O and CH_3OH , that can be used to model the shock chemistry and excitation conditions.

We thank Dirk Froebrich for useful discussions. We thank the referee, Alberto Noriega-Crespo, whose critical comments helped us to present a more complete and comprehensive picture of Cep E; in particular, for pointing out the presence of a second jet and suggesting using the IRAC colors. The research described in this paper was carried out at the Jet Propulsion Laboratory, California Institute of Technology, under a contract with the National Aeronautics and Space Administration. M. S. N. Kumar is supported by a Ciência 2007 contract, funded by FCT/MCTES (Portugal) and POPH/FSE (EC).

REFERENCES

- Aumann, H. H., Fowler, J. W. & Melnyk, M. 1990, *AJ*, 99, 1674
- Arce, H. G., & Sargent, A. I. 2006, *ApJ*, 646, 1070
- Arce, H. G., Shepherd, D., Gueth, F., Lee, C.-F., Bachiller, R., Rosen, A., & Beuther, H. 2007, in *Protostars and Planets V*, p2245
- Ayala, S., Noriega-Crespo, A., Garnavich, P., Curiel, S., Raga, A. C., Böhm, K. H., & Raymond, J. 2000, *AJ*, 120, 909
- Backus, C. R., Velusamy, T., Thompson, T. J., & Arballo, J. K. 2005, in *ADASS XIV, ASP Conference Series*, Vol. 347, p 61; P. L. Shopbell, M. C. Britton, and R. Ebert, eds.
- Bally, J. 2007, *Astrophysics & Space Science*, 311, 15
- Banerjee R., & Pudritz R. E. 2006, *ApJ*, 641, 949
- Bourke, T. L. et al. 2006 *ApJ*, 649, L37
- Cantó J., & Raga A. C. 1991, *ApJ*, 372, 646-658.
- Chapman, N. L., Mundy, L. G., Lai, S-P., & Evans, N. J., II. 2009, *ApJ*, 690, 496,
- Chiang, H-F., Looney, L. W., Tobin, J. J., & Hartmann, L. 2010, *ApJ* 709, 470
- Chini, R., Ward-Thompson, D., Kirk, J. M., Nielbock, M., Reipurth, B., & Sievers, A. 2001, *A&A*, 369, 155
- Codella, C., et al. 2010, *A&A*, 518, L112
- Combet, C., Lery, T., & Murphy, G. C. 2006, *ApJ*, 637, 798
- Devine, Reiputh & Bally 1997, *IAUS*, 182, 91
- Dionatos, O., Nisini, B., Cabrit, S., Kristensen, L., & Pineau des Ferts, G. 2010, *A&A* 521, A7
- Dionatos, O., Nisini, B., Garcia Lopez, R., et al. 2009, *ApJ*, 692, 1
- Eisloffel, J., Smith, M. D., Davis, C. J., & Ray, T. P. 1996, *AJ*, 112, 2086
- Forbrich, J., et al. 2010, 716,1453
- Forbrich, D. 2005, *ApJS*, 156, 169
- Forbrich, D., Smith, M. D., Hodapp, K. W., & Eisloffel, J. 2003, *MNRAS*, 346, 163
- Gredel, R., & Reipurth, B. 1993, *ApJL*, 407, L29
- Gramajo, L.V., Whitney, B. A., Gómez, M., & Robitaille, T. P. 2010, *AJ*, 139, 2504
- Gregersen, E. M., Evans, N. J., II, Mardones, D., & Myers, P. C. 2000, *ApJ*, 533, 440
- Hartigan, Raymond & Hartmann 1987, *ApJ*, 316, 323
- Hirano, N., Liu, S.-Y., Shang, H., et al. 2006, *ApJ*, 636, L141
- Indebetouw, R., Mathis, J. S., Babler, B. L., et al. 2005, *ApJ*, 619, 931
- Königl, A., & Pudritz, R. E. 2000, In *Protostars and Planets IV*, ed. V. Mannings, A. P. Boss, & S. S. Russell (Tucson: Univ. Arizona Press), 759
- Lee, C.-F., Hasegawa, T. I., Hirano, N., et al. 2010, *ApJ*, 713, 731
- Ladd, E. F., & Hodapp, K.-W. 1997, *ApJ*, 474, 749
- Lefloch, B., et al. 2010, *A&A*, 518, L113
- Looney, L. W., Tobin, J. J., & Kwon, W. 2007, *ApJ*, 670, L131
- Lucy, L. B. 1974 *AJ*, 79, 745
- Lery, T. 2003, *Ap&SS*, 287, 35
- Machida, M. N., Inutsuka, S-I., & Mastumoto, T. 2008, *ApJ*, 676, 1088
- Moro-Martín, A., Noriega-Crespo, A., Molinari, S., Testi, L., Chernicharo, J., & Sargent, A. 2001, *ApJ*, 555, 146
- Mundt, R., & Fried, J. W. 1983, *ApJ*, 274, L83
- Neufeld, D. A., & Yuan, Y. 2008, *ApJ*, 678, 974
- Neufeld, D. A., et al. 2006, *ApJ*, 649, 816
- Neufeld, D. A., et al. 2009, *ApJ*, 706, 170
- Nisini, B., Caratti o Garatti, A., Giannini, T., & Lorenzetti, D. 2002, *A&A*, 393, 1035
- Nisini, B., et al. 2010, *ApJ*, 724,69
- Noriega-Crespo, A., Garnavich, P M., Molinari, S. 1998, *AJ*, 116, 1388
- Noriega-Crespo, A., et al. 2004a, *ApJS*, 154, 352
- Noriega-Crespo, A., et al. 2004b, *ApJS*, 154, 402
- Noriega-Crespo, A., Hines, D. C., Gordon, K., Marleau, F. R., Rieke, G. H., Rho, J., Latter, W. B. 2009, in "The Evolving ISM in the Milky Way & Nearby Galaxies". online <http://ssc.spitzer.caltech.edu/mtgs/ismevol/>
- Ostriker, E. C., Lee, C., Stone, J. M., & Mundy, L. G. 2001, *ApJ*, 557, 443
- Ouyed, R., & Pudritz, R. E. 1997, *ApJ*, 482, 712
- Pudritz, R. E., Ouyed, R., Fendt, Ch., & Brandenburg, A. 2007, in *Protostars and Planets V*, p277
- Raga, A., & Cabrit, S. 1993, *A&A*, 278, 267
- Raga, A. C., Noriega-Crespo, A., Gonzalez, R. F., & Velazquez, P. F. 2004, *ApJS*, 154, 346
- Richardson, W. H. 1972 *J. Opt. Soc. Am.*, 62, 55
- Robitaille, T. P., Whitney, B. A., Indebetouw, R., & Wood, K. 2007, *ApJS*, 169, 328
- Rodríguez, L. F., et al. 1998, *Nature*, 395, 355
- Santiago-Garca, J., Tafalla, M., Johnstone, D., & Bachiller, R. 2009, *A&A*, 495, 169
- Shang, H., Allen, A., Li, Z.-Y., et al. 2006, *ApJ*, 649, 845
- Shepherd, D. S., Yu K. C., Bally J., & Testi L. 2000, *Astrophys.J.*, 535, 833-846.
- Smith, M. D., Froebrich, D., & Eisloffel, J. 2003, *ApJ*, 592,245
- Smith, M. D., & Rosen, A. 2005, *MNRAS* 357, 1370
- Smith, N., et al. 2010, *MNRAS*, 406, 952
- Stutz, A. M., Rubin, M., Werner, M. W., Rieke, G. H., Bieging, J. H., Keene, J., Kang, M., Shirley, Y. L., Su, K. Y. L., Velusamy, & T., Wilner, D. J. 2008, *ApJ*, 687, 389
- Shu, F. H., Najita, J. R., Shang, H., & Li, Z.-Y. 2000, in *Protostars and Planets IV*, ed. V. Mannings, A. P. Boss, & S. S. Russell (Tucson: Univ. Arizona Press), 789
- Tafalla, M., Santiago-Garca, J., Hacar, A., & Bachiller, R. 2010, *A&A* 522, 91
- Terquem, C., Eisloffel, J., Papaloizou, J. C. B., & Nelson, R. P. 1999, *ApJL*, 512, L131
- Tobin, J. J., Looney, L. W., Mundy, L. G., Kwon, W., & Hamidouche, M. 2007, *ApJ*. 659,1404
- Tobin, J. J., Hartmann, L., Calvet, N., & DAlessio, P. 2008, *ApJ*, 679, 1364
- Tobin, J. J., Hartmann, L., & Loinard, L. 2010, *ApJL*, 722, L12
- Tobin, J. J., Hartmann, L., Looney, L. W., & Chiang, H.-F. 2010, *ApJ*, 712, 1010
- Torrelles, J. M. T., et al. 2011, *MNRAS*, 410, 627
- Velusamy, T. & Langer, W. D. 1998, *Nature* 392, 686
- Velusamy, T., Langer, W. D., Marsh, K. A. 2007 *ApJL*, 668, L159
- Velusamy, T., Marsh, K. A., Beichman, C. A., Backus, C. R., & Thompson, T. J. 2008, *AJ* 139, 197
- Watson, C., Zweibel E. G., Heitsch F., & Churchwell E. 2004, *ApJ*, 608, 274-281.
- Whitney, B. A., Wood, K., Bjorkman, J. E., & Cohen, M. 2003a, *ApJ*, 598, 1079
- Whitney, B. A., Wood, K., Bjorkman, J. E., & Wolff, M. J. 2003b, *ApJ*, 591, 1049
- Ybarra, J. E., & Lada, E. A. 2009, *ApJL*, 695, L123
- Yu, K. C., Billawala, Y., & Bally, J. 1999, *AJ*, 118, 2940

TABLE 1
OBSERVED PROTOSTAR PARAMETERS FROM THE HiRES MAPS

Band μm	Peak MJy sr^{-1}	size " \times "	Flux density Jy
3.6	355	0.83×0.72	0.0055
4.5	1877	0.73×1.00	0.0358
5.8	6465	0.71×0.91	0.111
8.0	10964	0.78×0.85	0.196
24	47597	1.97×2.06	5.15
70	32714	5.23×6.03	26.4

TABLE 2
RESULTS FROM SED MODELING: PROTOSTAR

Age $\log(\text{yr})$	M_* $\log(M_\odot)$	R_* $\log(R_\odot)$	T_* $\log(T_\odot)$
4.33 ± 0.1	0.51 ± 0.01	1.24 ± 0.01	3.64 ± 0.00

TABLE 3
RESULTS FROM SED MODELING: DISK AND ENVELOPE

\dot{M}_{env} $\log(M_\odot \text{yr}^{-1})$	R_{Max}^{env} $\log(\text{AU})$	M_{disk} $\log(M_\odot)$	R_{Max}^d $\log(\text{AU})$	\dot{M}_{disk} $\log(M_\odot \text{yr}^{-1})$	incl °	M_{env} $\log(M_\odot)$
-3.85 ± 0.14	4.07 ± 0.09	-2.17 ± 0.73	1.82 ± 0.39	-7.53 ± 0.52	42 ± 17	0.87 ± 0.28

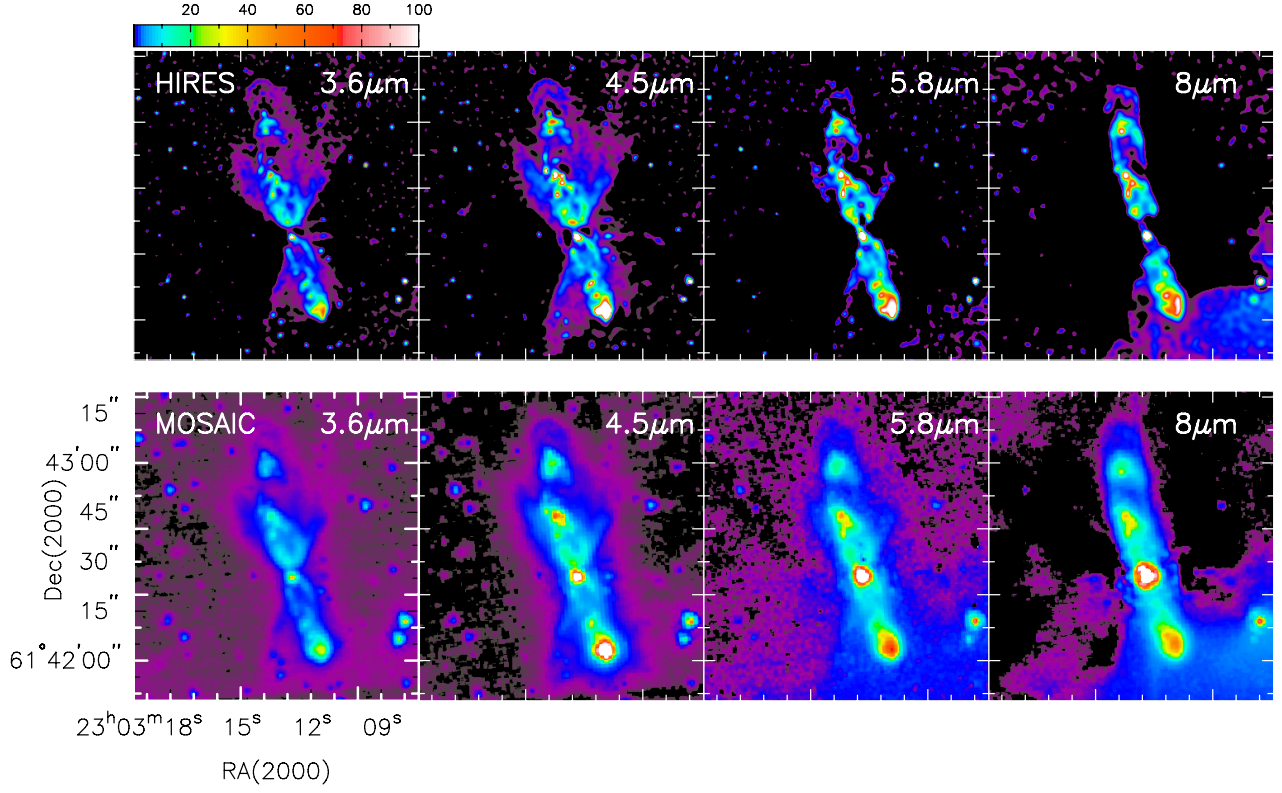


FIG. 1.— Mosaic (lower) and HiRes deconvolved (upper) images in the IRAC bands. In all images the color stretch and the square root scaling used are designed to bring out the low surface emissions and thus the brightest emission is saturated. It is readily evident that the image enhancement in the HiRes images improves the visualization of the morphologies of jets and outflows by virtue of the increase in the resolution to sub-arcsec scale, and by removal of the confusion from the “side-lobes”.

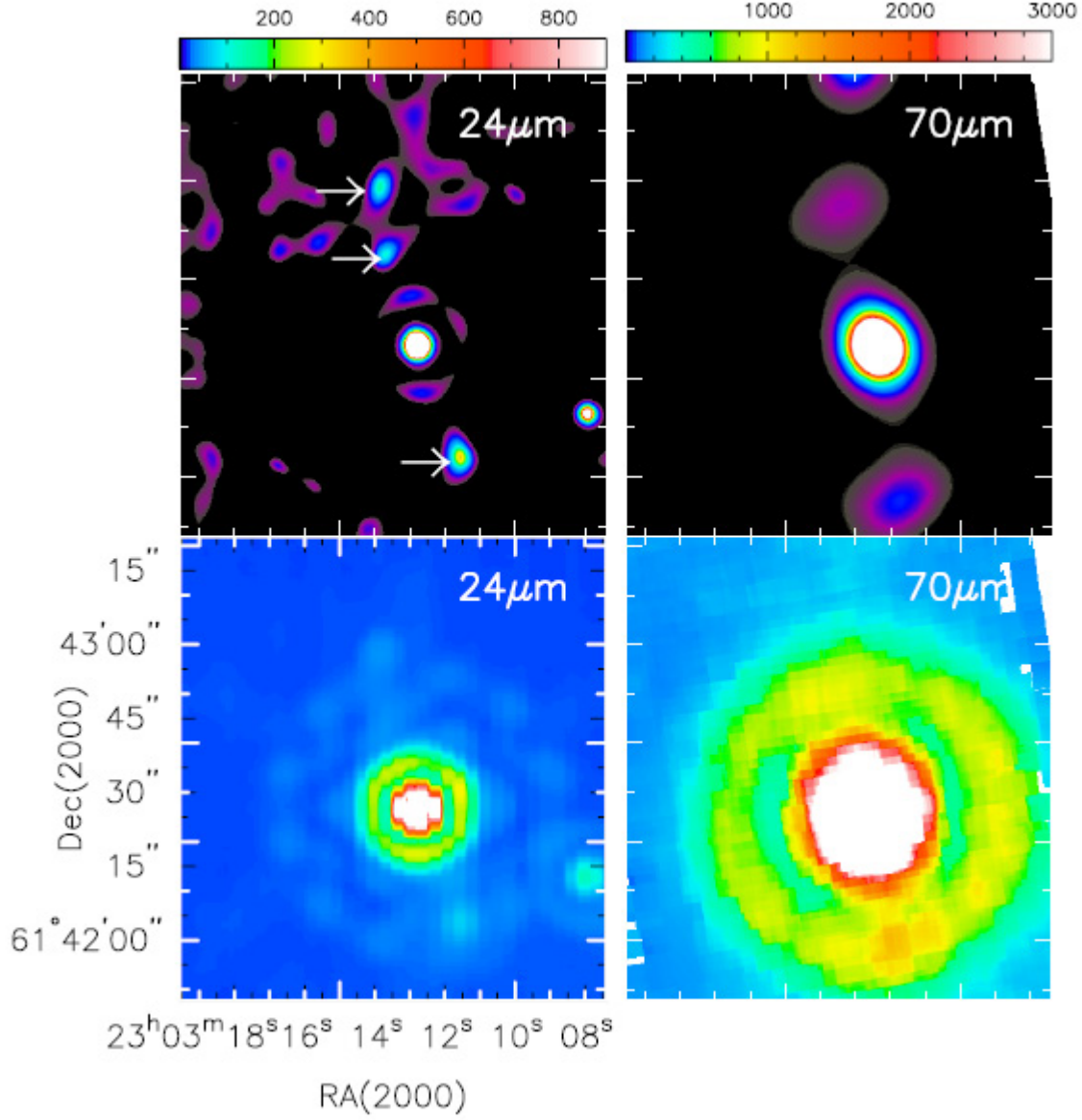


FIG. 2.— Mosaic (lower) and HiRes deconvolved (upper) images in the MIPS bands. The arrows in the 24 μm HiRes image indicate the features which are distinctly visible only after the HiRes processing and were formerly completely masked by the “side-lobes” in the mosaic image.

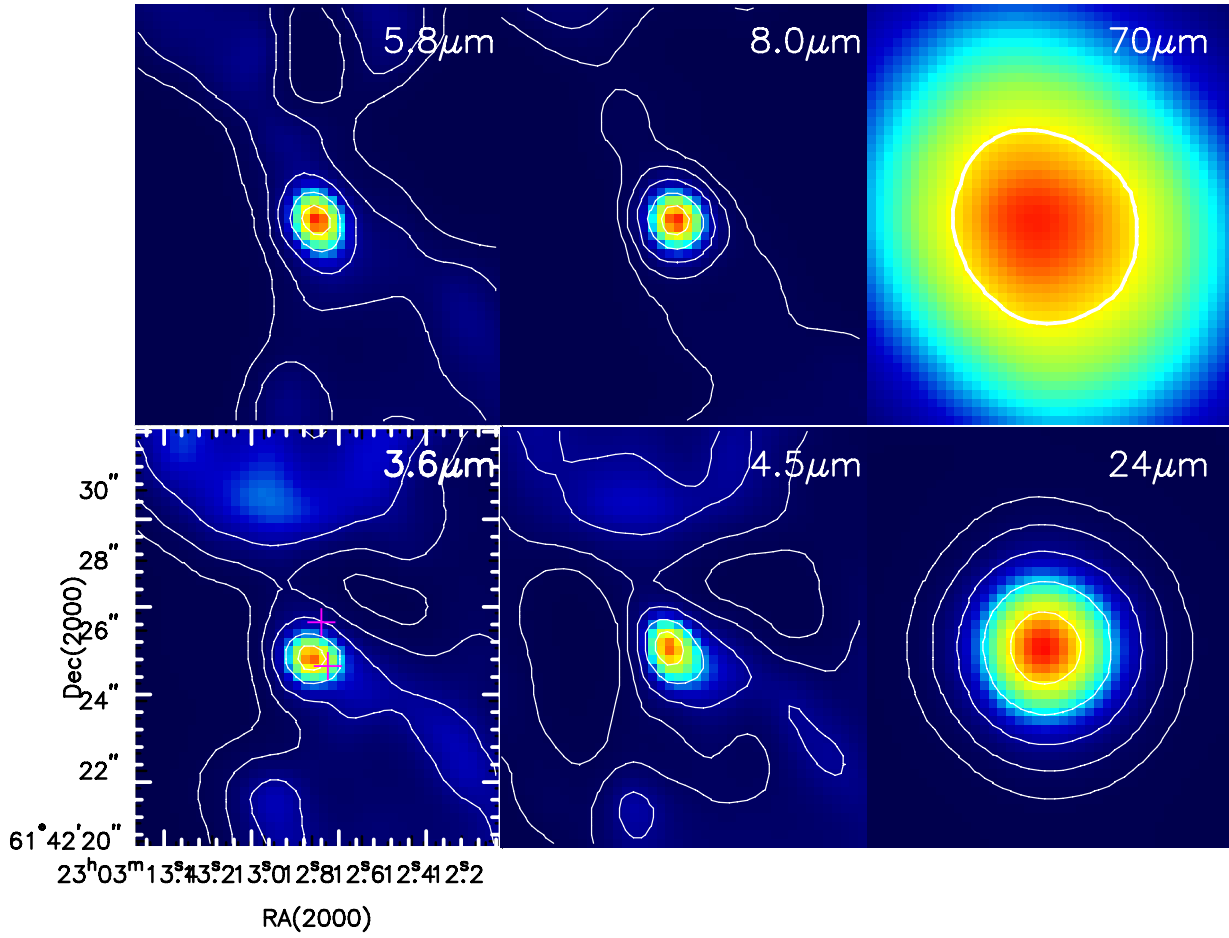


FIG. 3.— HiRes maps of the inner 10'' region around the Cep E protostar. The contour levels are at 0.01%, 0.1%, 1%, 10% and 50% of the peak intensity (listed in Table 1) at each band. At 70 μm only the contour at 50% peak intensity is plotted. Note the extremely low surface brightness of the outflow-jet features in all IRAC bands, delineated by the low-level contours at intensities below a few percent of the peak at the protostar. The crosses in the 3.6 μm map represent the positions of the mm double source (from Moro-Martín et al. 2001).

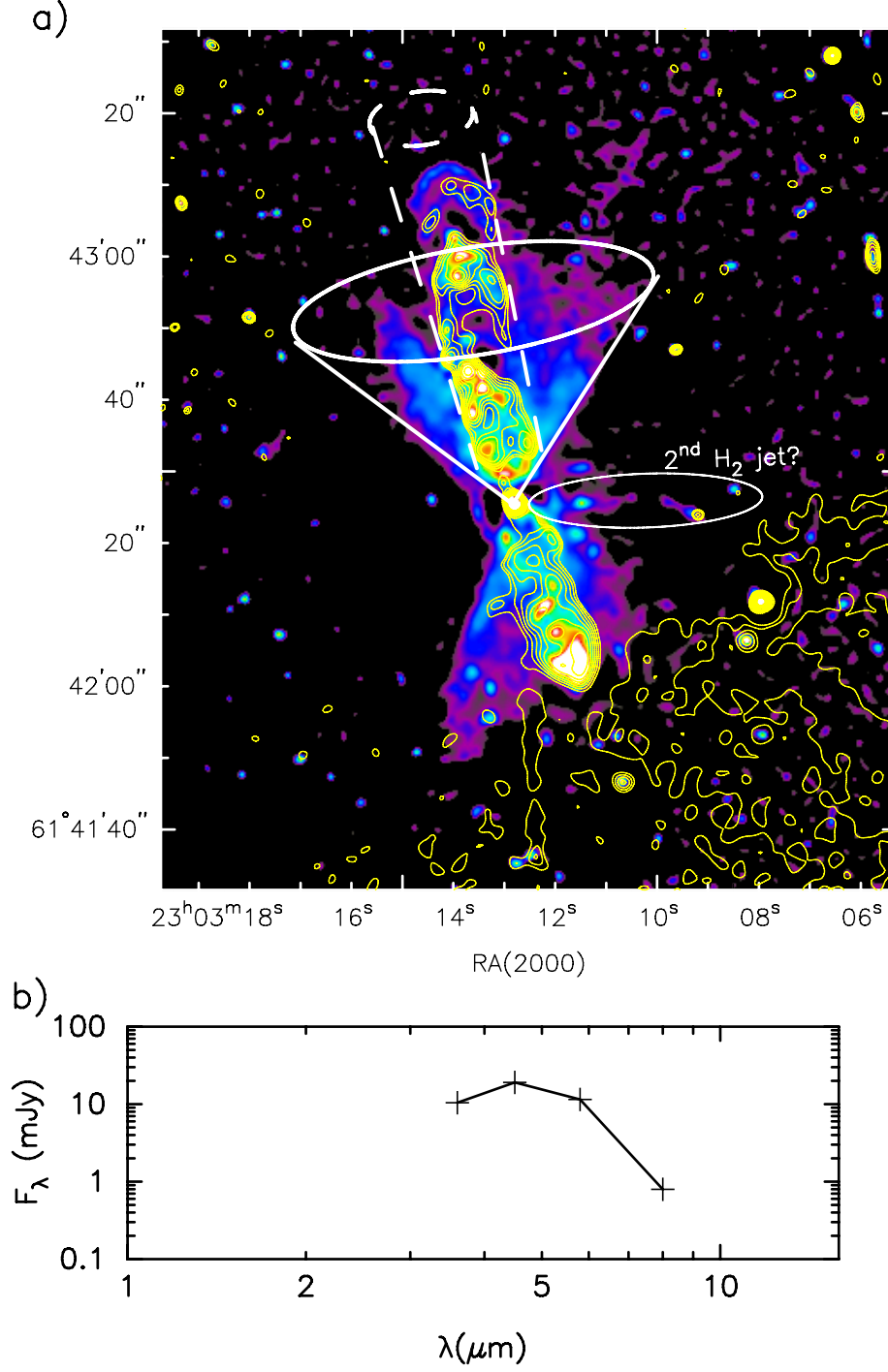
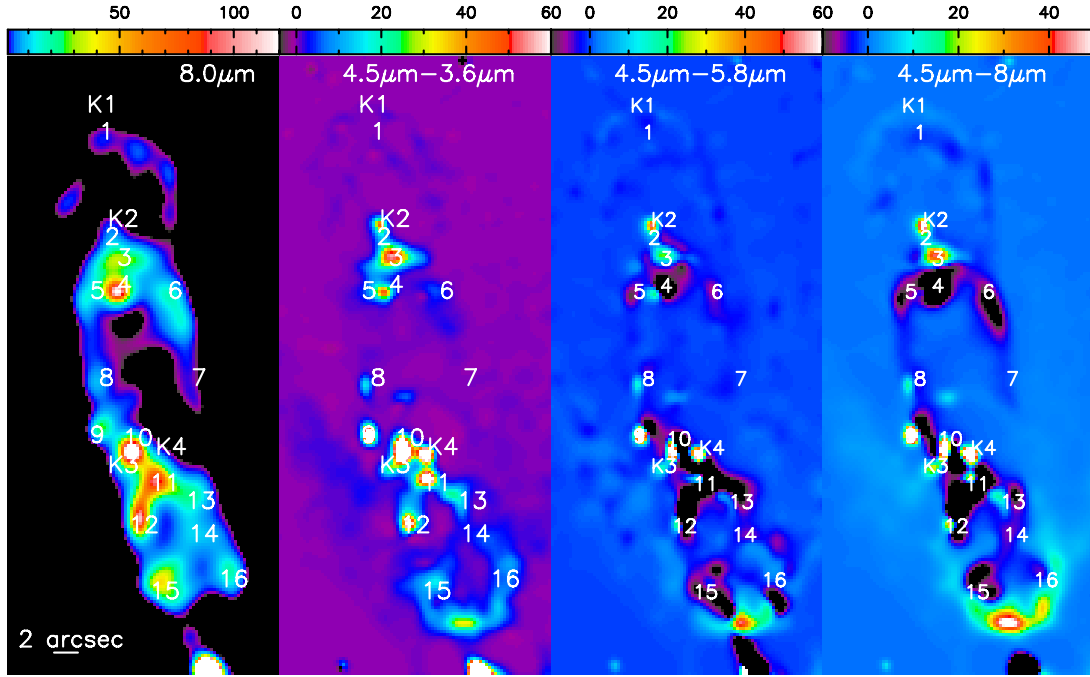


FIG. 4.— (a) The 8 μm emission (intensity contours) tracing the jet overlaid on the 4.5 μm image which traces both the jet and the wide angle outflow in scattered light. The contour intensities are at 1, 2, 4, 8, 16, 32, 64, 128 and 256 MJy sr^{-1} (peak intensity is 10,964 MJy sr^{-1}). We show a schematic of the bi-conical wide angle outflow (solid lines) and the narrow jets and associated bowshocks (broken lines) in the northern lobe. The plausibility of a second H₂ molecular jet/outflow (see text) is indicated. (b) Spectral plot of relative intensities of the scattered light integrated over the area between the boundaries of the wide angle outflow and the narrow jet as shown in the upper panel.

a) NE lobe



b) SW lobe

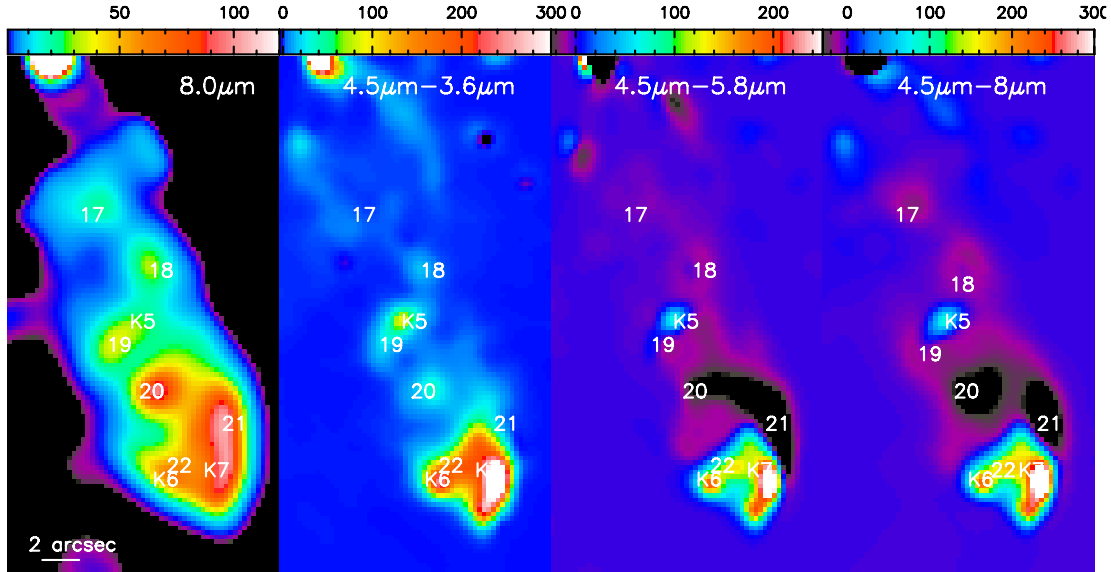


FIG. 5.— The $8\ \mu\text{m}$ image (left panel), and difference images between IRAC bands (right three panels) showing the spatial variation of excitation across the bowshocks inferred from the colors: (a) NE lobe; (b) SW lobe. In H_2 a total of 29 jet features, “knots”, are identified as marked on the images in all panels. The numbered labels 1 to 22 represent the knots identified by the peak emissions in the $8\ \mu\text{m}$ image. The knots identified by K1 to K7 represent those less prominent at $8\ \mu\text{m}$ but are bright at $4.5\ \mu\text{m}$.

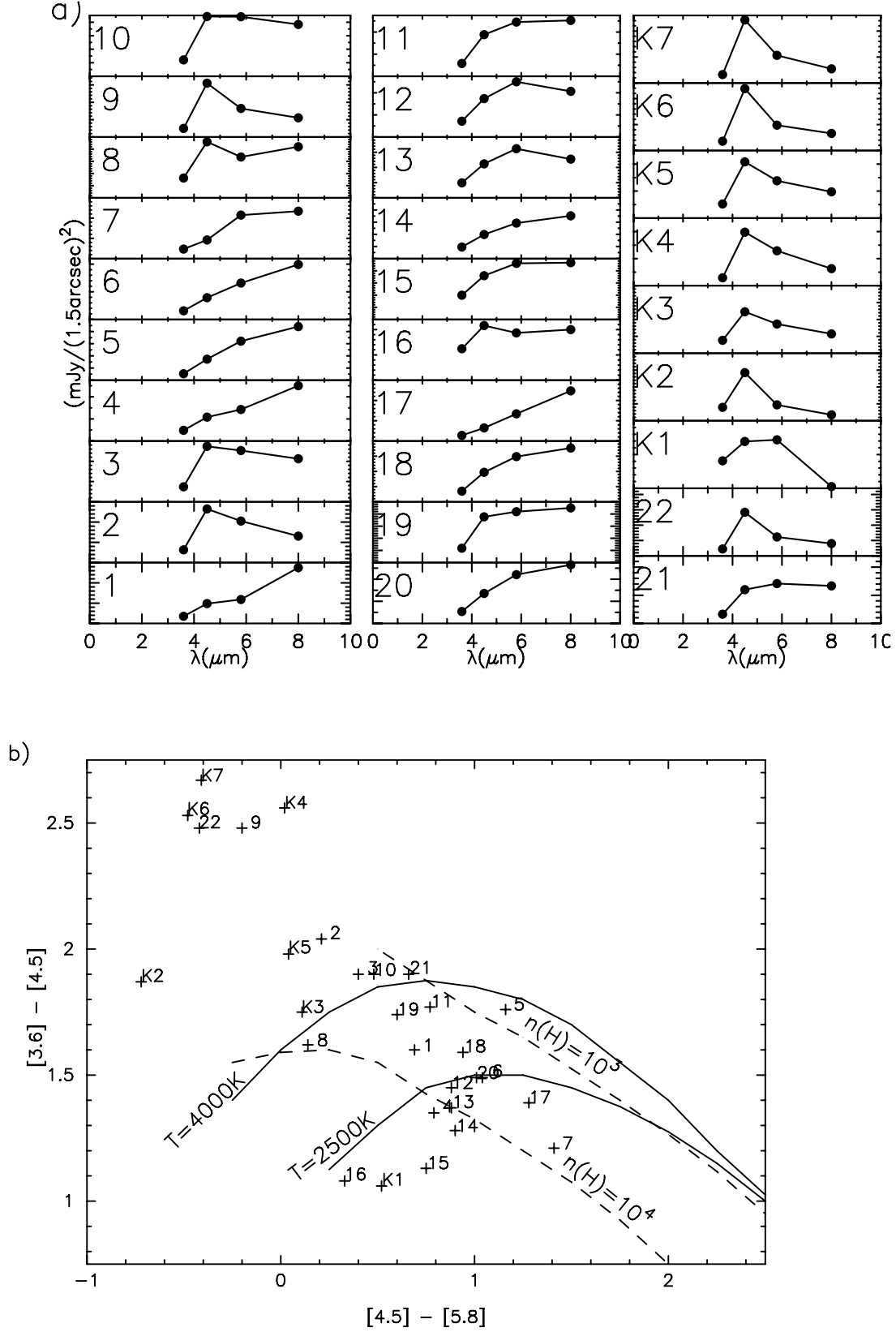


FIG. 6.— (a) Flux density spectral plots of the knots; the labels refer to the position of the knots as marked on Figs. 5a & 5b (see text). (b) IRAC color-color plot for the knots identified in Figs. 5a & 5b. The numbered labels identify the knots. The constant temperature (solid lines) and density (broken lines), reproduced from Ybarra & Lada (2009), represent statistical equilibrium model calculations of IRAC colors for H_2 gas in the shocks.

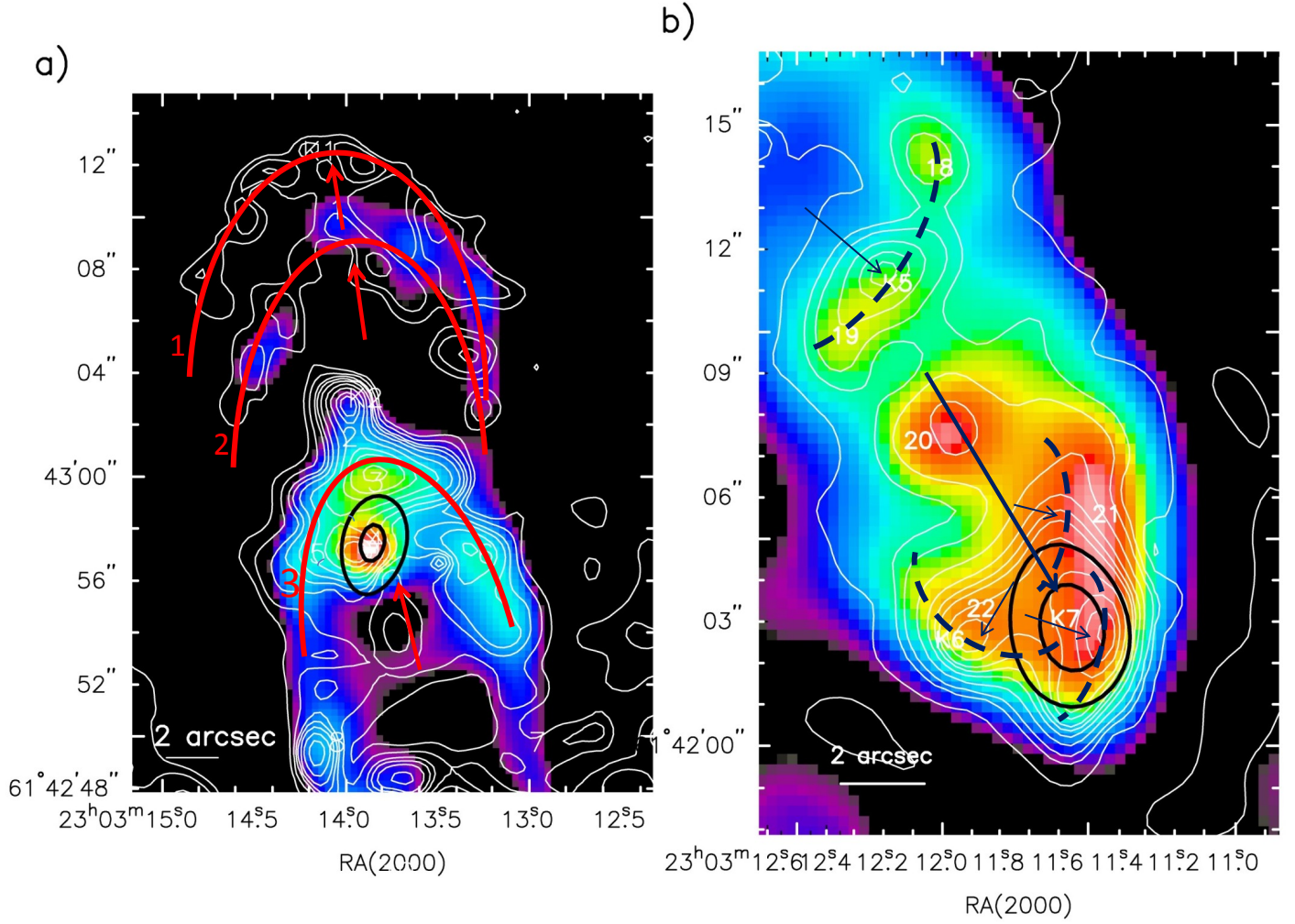


FIG. 7.— The 4.5 μm intensity contours (white) overlaid on 8 μm emission (color image) showing the relative displacement between them. The MIPS 24 μm emission (tracing the atomic gas in the jet head/J- shocks) is shown by selected solid black contours (near peak and half power intensities). (a) Tip of NE lobe. Red arcs show a schematic of three bowshocks as inferred from 4.5 μm emissions. (b) Tip of SW lobe showing a complex system of oblique C-type shocks. The arcs (dashed lines) represent leading edges of C-type shocks as inferred from the 4.5 μm emissions. The short arrows mark the “putative” projected oblique shock directions as “inferred” from the viewing geometry and the relative displacement between 8 μm and 4.5 μm intensities (see text). The long arrow marks the direction of the atomic jet.

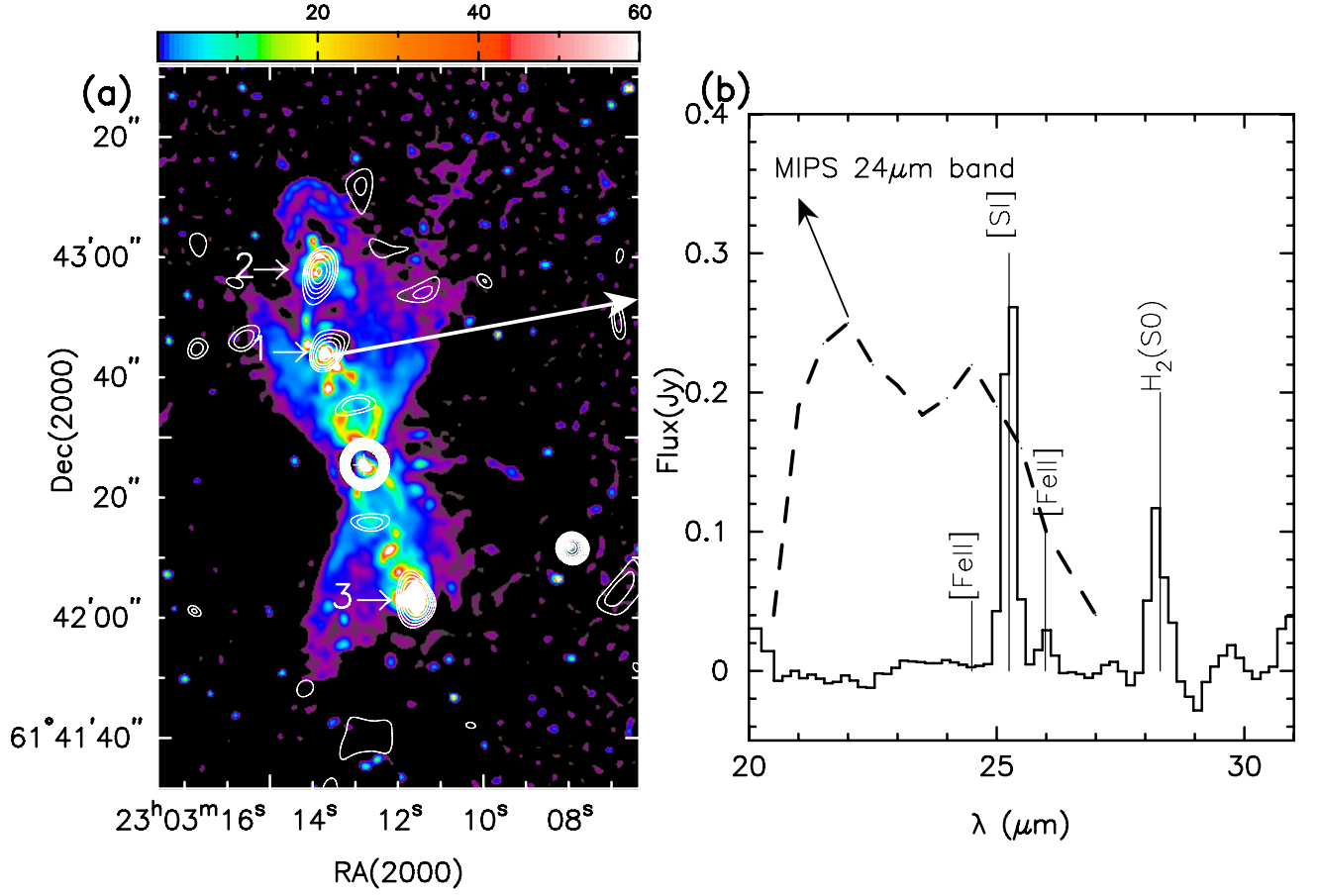


FIG. 8.— (a) 24 μm emission (contours) overlaid on the 4.5 μm image. The intensity contours are at 4, 8, 16, 32, 64, 128, 256, 512, and 1024 MJy sr^{-1} . The contours near the center represent the protostar with a peak intensity of 47,597 MJy sr^{-1} . The long arrow marks the emission feature for which the IRS spectrum is shown. The labels 1 to 3 mark the 24 μm emission peaks along the jet. (b) IRS LL spectrum of the 24 μm NE emission peak (labeled #1). The atomic/ionic spectral features are marked. The MIPS 24 μm band response is also shown.

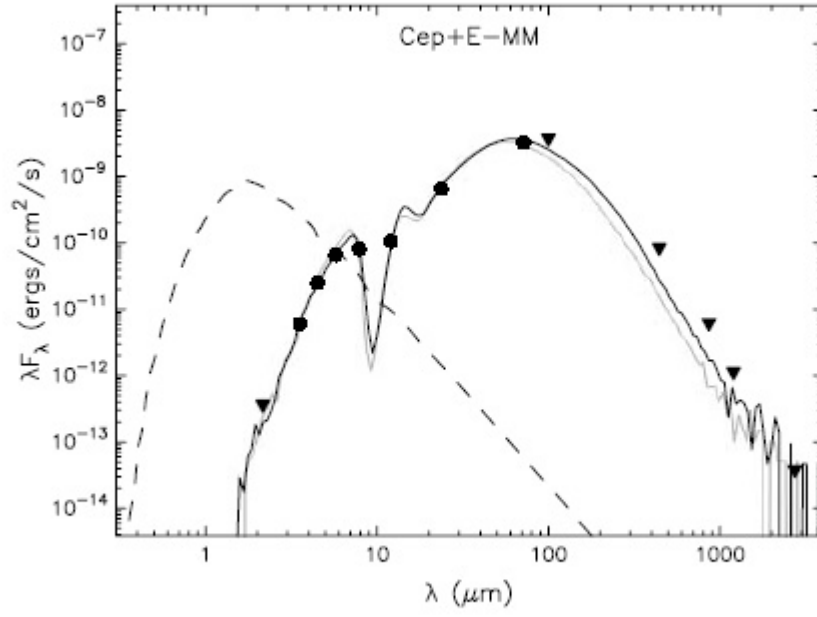


FIG. 9.— SED fitting for the Cep E protostar. The solid black line shows the best fitting model. Grey lines show the models that satisfy the criteria $\chi^2 - \chi^2_{best} < 3$. Black dots are data points and triangles are upper limits. The dashed line shows the stellar photosphere of the best fit model.

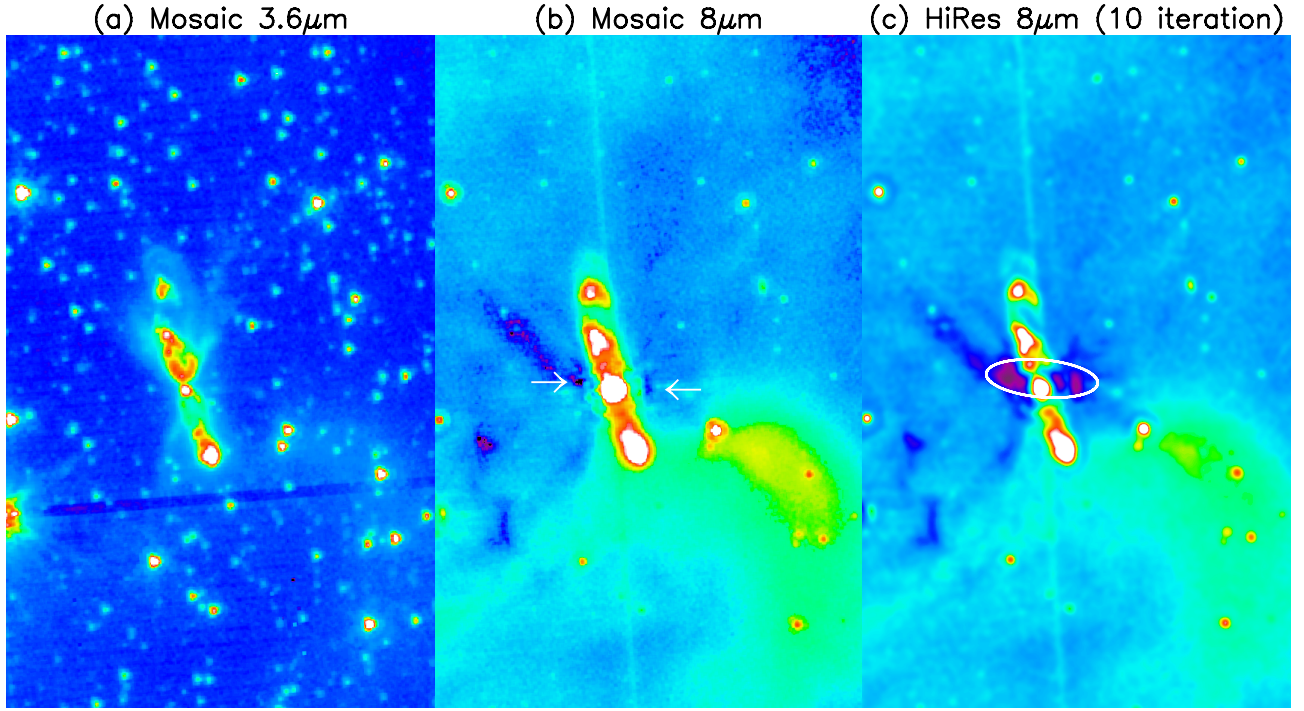


FIG. 10.— Extinction at 8 μm through a dense envelope surrounding the protostar. Mosaic images of a large region around the protostar showing the interstellar background at 3.6 μm (panel a) and at 8 μm (panel b); the arrows (in panel b) mark extinction near the protostar. (c) The 8 μm HiRes deconvolved image after 10 iterations, processed without background subtraction (see text). The ellipse indicates the flattened envelope region with high extinction at 8 μm .